



Society for Science and Education
United Kingdom

ISSN: 2055 - 1266
Volume 5 No 2
April 2018

JOURNAL OF BIOMEDICAL ENGINEERING AND MEDICAL IMAGING

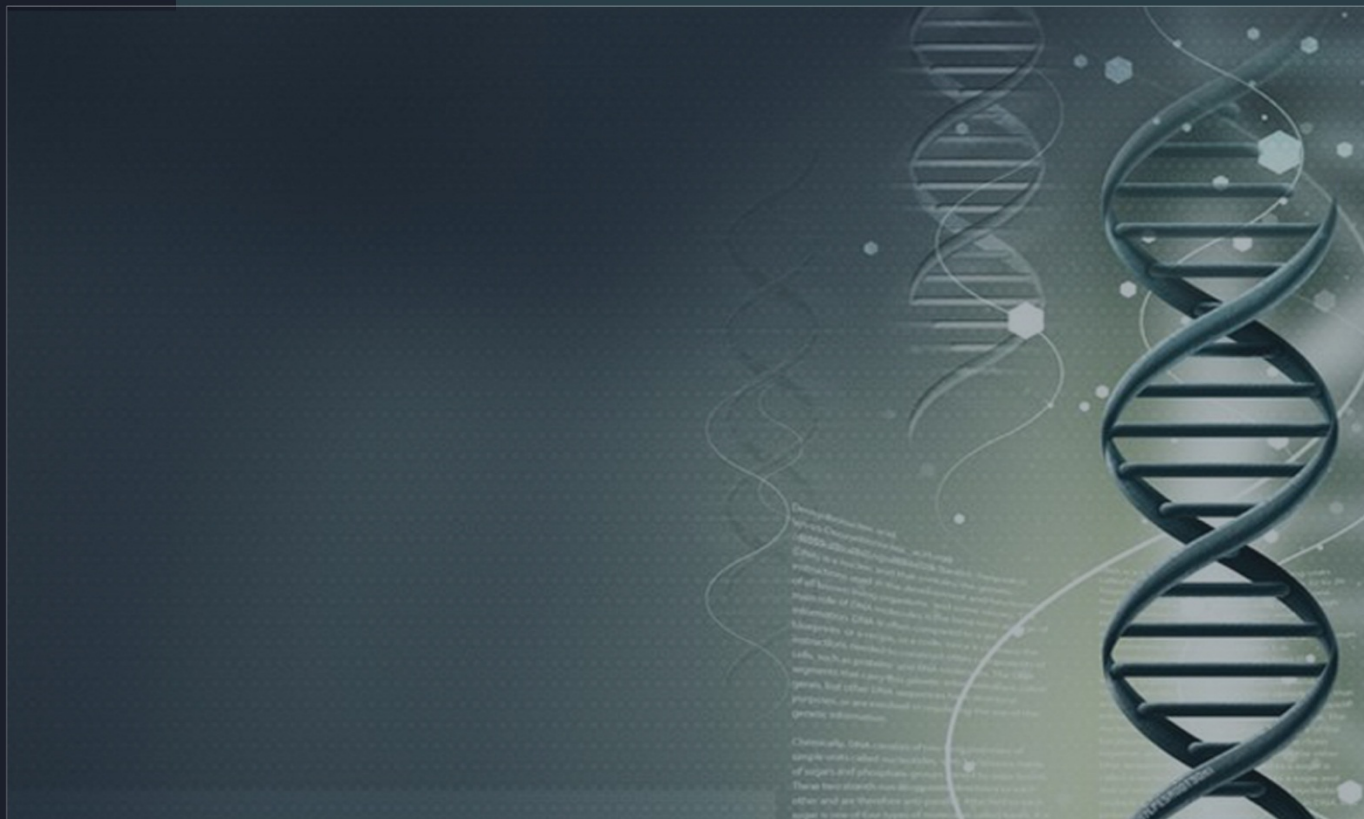


TABLE OF CONTENTS

EDITORIAL ADVISORY BOARD	I
DISCLAIMER	II
The Mathematical Model for Drug Delivery Through Skin Nourelhoda Medhat Mahmoud, Ziad Tarek Alshafee	1
Automated 3-D Tissue Segmentation via Clustering S. Edwards, S. Brown, M. Lee	8
Calculation of Inversion Time (TI) value for Fat Suppression in the Modified Spin Echo Sequence Method. Sunil Kalagi	21
Comparative Study of Left Ventricular Low Wall Motion with Scar Tissue Using 4D Left Ventricular Cardiac Images Chien-Yi Lee, Yashbir Singh, Michael Friebe, Wei-Chih Hu	29
External Group Labeling of Objects in 2D Medical Images Using Spring-Mass Model Muhammad Masud Tarek, Bilkis Jamal Ferdosi	40

EDITORIAL BOARD

Editor-in-Chief

Prof. Kenji Suzuki

Department of Radiology, University of Chicago
United States

Members

Prof. Habib Zaidi

Dept. of Radiology, Div. of Nuclear Medicine
Geneva University Hospital, Geneva
Switzerland

Prof. Tzung-Pe

National University of Kaohsiung, Taiwan
China

Prof. Nicoladie Tam

Dept. of Biological Sciences, University of North Texas
United States

Prof. David J Yang

The University of Texas MD Anderson Cancer Center, Houston
United States

Prof. Ge Wang

Biomedical Imaging Center
Rensselaer Polytechnic Institute Troy, New York
United States

Dr Hafiz M. R. Khan

Department of Biostatistics, Florida International University
United States

Dr Saad Zakko

Director of Nuclear Medicine Dubai Hospital
UAE

Dr Abdul Basit

Malaysia School of Information Technology, Monash
University
Malaysia

Prof. Christian L. Althaus

University of Bern
Switzerland

Prof. Zandrea Ambrose

University of Pittsburgh
United States

Prof. Anthony S Amend

University of Hawaii at Manoa
United States

Prof. Antonio Amorim

Universidade do Porto
Portugal

Prof. William Amos

University of Cambridge
United Kingdom

Prof. Rachel L. Allen

University of London
United Kingdom

Prof. Heike Allgayer

University of Heidelberg
Germany

Prof. Virginia Abdala

UNT-CONICET
Argentina

Prof. Robert B Abramovitch

Michigan State University
United States

Prof. Arti Ahluwalia

University of Pisa
Italy

Prof. Maria Cristina Albertini

University of Urbino
Italy

Dr. Virginia Abdala

UNT-CONICET
Argentina

Dr. Jafri M. Abdullah

Fellow of the Academy of Sciences, Universiti Sains
Malaysia

Prof. Robert B Abramovitch

Michigan State University
United States

Dr. Irina U Agoulnik

Florida International University College of Medicine
United States

Prof. Arti Ahluwalia

University of Pisa
Italy

Dr. Sonja-Verena Albers

University of Freiburg
Germany

Prof. Maria Cristina Albertini

University of Urbino
Italy

Prof. SUnited Statesn C Alberts

Duke University
United States

Prof. Dawn N Albertson

Minnesota State University, Mankato
United States

Dr. Silvia Alessi-Severini

University of Manitoba
Canada

Dr. Veerasathpurush Allareddy

University of Iowa
United States

Prof. Patrick Aloy

Institute for Research in Biomedicine
Spain

Prof. Gerhard Andersson

Linkoping University
Sweden

Prof. Nigel R. Andrew

University of New England
United Kingdom

Prof. Martin Anger

Central European Institute of Technology (CEITEC)
Czech Republic

Prof. Maria Anisimova

Zurich University of Applied Sciences
Switzerland

Prof. Jérémy Anquetin

JURASSICA Museum in Porrentruy
Switzerland

Prof. Praveen Arany

University at Buffalo
United States

Dr. Ignacio Arganda-Carreras

Ikerbasque, Basque Foundation for Science
Spain

Prof. Irina U Agoulnik

Florida International University College of Medicine
United States

Prof. Sonja-Verena Albers

University of Freiburg
Germany

Prof. Silvia Alessi-Severini

University of Manitoba
Canada

- Prof. Rachel L. Allen**
University of London
United Kingdom
- Prof. Heike Allgayer**
University of Heidelberg
Germany
- Prof. Patrick Aloy**
Institute for Research in Biomedicine
Spain
- Prof. Christian L. Althaus**
University of Bern
Switzerland
- Prof. Antonio Amorim**
Universidade do Porto
Portugal
- Prof. Gerhard Andersson**
Linköping University
Sweden
- Prof. Martin Anger**
Central European Institute of Technology (CEITEC)
Czech Republic
- Prof. Maria Anisimova**
Zurich University of Applied Sciences
Switzerland
- Prof. Louise Barrett**
University of Lethbridge
Canada
- Prof. Kerstin Bartscherer**
Max Planck Institute for Molecular Biomedicine
Germany
- Dr. Ugo Bastolla**
Universidad Autónoma de Madrid
Spain
- Prof. Amanda E Bates**
University of Southampton
United Kingdom
- Prof. Isabel Bäurle**
University of Potsdam
Germany
- Prof. Gerrit T.S. Beemster**
University of Antwerp
Belgium
- Prof. Maria del Mar Bibiloni Esteva**
University of the Balearic Islands
Spain
- Prof. Kate N Bishop**
The Francis Crick Institute
United Kingdom
- Prof. Ton Bisseling**
Wageningen University
Netherlands
- Prof. Anne Blangy**
Montpellier University
France
- Prof. Marnie E Blewitt**
The Walter and Eliza Hall Institute of Medical Research
Australia
- Prof. Anna M. Borghi**
University of Bologna
Italy
- Prof. Bettina Böttcher**
Bayerische Julius-Maximilians-Universität Würzburg
Germany
- Prof. Jürgen C Becker**
Medical University of Graz
Austria
- Prof. Laura M Boykin**
The University of Western Australia
Australia
- Prof. Ignacio Arganda-Carreras**
Ikerbasque, Basque Foundation for Science
Spain
- Prof. Nebojsa N Arsenijevic**
University of Kragujevac
Serbia
- Prof. Spyros Artavanis-Tsakonas**
Harvard Medical School
United States
- Prof. Ramy K Aziz**
Faculty of Pharmacy, Cairo University
Cairo
- Prof. Thomas Backhaus**
University of Gothenburg
Sweden
- Prof. Nicholas A Badcock**
Macquarie University
Australia
- Prof. Elena E Bagley**
University of Sydney
Australia
- Prof. Vladimir B Bajic**
King Abdullah University of Science and Technology (KAUST)
Saudi Arabia
- Dr. Stefan D Baral**
Johns Hopkins School of Public Health
United States
- Prof. Tom Bourne**
Imperial College, London
United Kingdom
- Prof. Sheila M. Bowyer**
University of Pretoria
South Africa
- Prof. Mark Boyes**
Curtin University of Technology
Australia
- Prof. Erika M Braga**
Federal University of Minas Gerais (UFMG)
Brazil
- Prof. Ebba Brakenhielm**
Rouen University
France
- Prof. Paolo Brambilla**
University of Udine
Italy
- Prof. Vincenzo Brancaleone**
University of Naples Federico II
Italy
- Prof. Björn Brembs**
Universität Regensburg
Germany
- Prof. Fiona S. Brinkman**
Simon Fraser University
Canada
- Prof. Jon Brock**
Macquarie University
Australia
- Prof. Eoin L. Brodie**
Lawrence Berkeley National Laboratory
United States
- Prof. Jacqueline Batley**
University of Western Australia
Australia
- Prof. Peter D Baade**
Cancer Council Queensland
Australia

DISCLAIMER

All the contributions are published in good faith and intentions to promote and encourage research activities around the globe. The contributions are property of their respective authors/owners and the journal is not responsible for any content that hurts someone's views or feelings etc.

The Mathematical Model for Drug Delivery Through Skin

¹Nourelhoda Medhat Mahmoud, ²Ziad Tarek Alshafee

¹Biomedical Engineering Department, Faculty of Engineering, Minia University, Minia, Egypt;

¹nourelhoda.mahmoud@mu.edu.eg; ²e-01205297@s-mu.edu.eg

ABSTRACT

Delivery of the medications is one of the important biomedical applications. It has significant importance for patients. There are a lot of methods for delivery of drugs such as oral, topical, sublingual, inhalation, and nasal and injection routes. Patients are suffering from needles every time they want to take their medications. The oral route is suitable and has the lowest cost, but some drugs can cause gastrointestinal tract irritation and has low bioavailability. Delivery of the medications through skin is the most suitable for patient because it is needleless without any pain for patients. Some medications have large size. Mathematical model for transportation of large molecules of medications and drugs through the skin is described. This model provides a significant reduction of medical complications and improvement in patient compliance. One of the most important parameter is the optimization of the response time of this model. The model shows good stability and response.

Keywords: Biomedical Applications; Medications; Mathematical model; Patients; Skin.

1 Introduction

Medications are very important to patients, they used for diagnosing, treatment, or preventing illness. There are many routes for medications delivery such as oral, topical, sublingual, inhalation, and injection. The most used methodologies for medications delivery are the oral and injection routes, but injection is painful for patients [1-7].

The oral route is the most suitable and has the lowest cost [8, 9]. Some drugs can cause gastrointestinal tract irritation.

The injection route encompasses intravenous (IV), intramuscular (IM), and subcutaneous (SC) administration [10]. Injections act rapidly, with onset of action in 15–30 seconds for IV, 10–20 minutes for IM, and 15–30 minutes for SC [11]. Disadvantages of injections include pain for the patient, and the requirement of trained staff. A hypodermic needle is used for rapid delivery of liquids, or when the injected substance cannot be ingested, such as with insulin because it cannot be absorbed [12, 13].

Jet injection uses the principle of application of high velocities. This principle is such that the drug formulation is propelled from the reservoir at a high speed, bombarding the skin surface and abrading it then creating superficial micro pathways in the skin. The injection of medications using jet affects flow by increasing velocity, decreasing pressure, and increasing momentum. The penetration using the jet damages the skin with its diameter but less than damage of needle [14-16].

DOI: 10.14738/jbemi.52.4252

Publication Date: 25th March 2018

URL: <http://dx.doi.org/10.14738/jbemi.52.4252>

The diffusion of medications and drugs through the skin is preferable to injection because it is non-invasive and can be self-administered. This results in a significant reduction of medical complications and improvement in patient compliance. The diffusion is the movement of the solute from high to low concentrations of the solute in the solvent. The microparticles in the fluid are affected by the diffusion force and it will be move based on this force. In general, a small particle diffuses faster than a larger one [17-20].

Transdermal patch is used for systemic delivery. It uses a micro needle which penetrate outer layer of skin then let solution to diffuse to lower layers through the new pores generated by micro needles [20, 21].

In this paper, mathematical model for transportation of medications and drugs through the skin without pain is described. This model provides a significant reduction of medical complications and improvement in patient compliance. This mathematical model uses medical principle for hypoproteinemia according to abnormality of hydrostatic pressure and principles of mass transfer through a porous diaphragm.

Hypoproteinemia is common complication of Nephrotic Syndrome. Nephrotic Syndrome is not a specific illness, but a group of clinical manifestations relate with kidney. Healthy kidneys regulate blood pressure, secrete hormone and purify blood. When kidneys are damaged, they will fail to do these jobs well, because of a series of symptoms appear. Hypoproteinemia refers to a condition where there is an abnormally low level of protein in the blood. In normal condition, when blood flows through kidney, some substances like protein can be kept in the body. However, when kidney structure is damaged, protein will leak into urine and thus form proteinuria. Long-term and severe protein leakage results in hypoproteinemia easily. One of main cause of this disease is hyper blood pressure which increase hydrostatic glomeruli pressure (HGP). This leads to pass of high molecular weight proteins according to increase diameter of pores [14, 22-24].

2 Mathematical Methodology

The proposed mathematical model for transportation of medications and drugs through the skin provides a significant reduction of medical complications and improvement in patient compliance. This model uses medical principle for hypoproteinemia according to abnormality of hydrostatic pressure and principles of mass transfer through a porous diaphragm.

For applying this model, there are three mainly steps:

- 1- Increase the diameter of skin pores by using a specific value of hydrostatic pressure come from blower and controlled by a valve (according to molecular weight of drug), the new pores will be in a very small scale (molecules scale).
- 2- Transportation of the drug solution through new pores and control the rate of the transportation by hydrostatic pressure (could be critical one or higher with limits to control damage).
- 3- Skin recovery: The skin recovery is a property of skin which enables pores to get its original diameter. With small scale, the recovery period will be very small.

2.1 Mechanism

As the main mechanism of nephron in kidney, the mechanism should include hydrostatic pressure source, making suitable pores of diaphragm (skin), inner design, and controlling from all sides (power source, on and off, pressure).

1. Hydrostatic pressure source

It will be from a microblower. The blower is considered as the source for the required force.

$$F=P/A \quad (1)$$

Where: F is the required force, P is the hydrostatic pressure, and A is the cross-section area.

The specs of the microblower that be used are: Pressure is up to 1.5 Kpa, Dimension is 20 x 20 x 1.8 mm, Power is from 10 to 20 V.

2. Inner design:

As shown in Figure 1, one-way valve is used as a safety valve and helps in keeping pressure constant, isolator is considered as mass (m) used to prevent blower air from mixing with solution, solution storage is used to keep a specific amount of solution, and skin interface is considered as a non-invasive interface with skin.



Figure 1. The schematic of the proposed model.

Solution passing through skin is represented as dumper (as in the principle of mass transfer) with gamma factor because they have the same principal. Gamma is considered as overall factors and it represents diffusion constant, skin conditions, and any other effective factors. Gamma can be calculated experimentally and given for user as a numerical value. Therefore, change in the distance (X) can be calculated. It represents the dosage.

3- Microcontroller

Any microcontroller will be used such as Arduino, arm or raspberry pi to control two main things:

Turn on blower for a specific duration till reach a specific pressure then turn off the blower.

Opening the valve to get back the pressure to its normal state after finishing of injection and as a safety for pressure.

In addition, microcontroller will be used for controlling the sensor, showing results, and user interface.

4- Transfer function and the mathematical model

$$Z = ms^2 + \gamma s \quad (2)$$

Where Z is mechanical impedance, M is isolator mass in (Kg), and γ is injection factor in (N.s/m).

The injection factor γ is related to effective condition of skin (as surface area, physical conditions of skin, type of drug, position of injection etc.). This factor could be measured experimentally then its range become a given to user in manual of device.

$$T.F = \frac{X(s)}{F(s)} = \frac{1}{ms^2 + \gamma s} \quad (3)$$

Where X is output distance in (m), F is input force in (N).

Assume the input force (F) from blower could be represented as unit step function with a gain K.

By compensation at equation (3);

$$X(s) = \frac{K}{s(ms^2 + \gamma s)} \quad (4)$$

$$X(s) = \frac{K}{s^2(ms + \gamma)} = \frac{K/\gamma}{s^2(1 + \frac{m}{\gamma}s)} \quad (5)$$

$$X(s) = \frac{K}{\gamma} \left(\frac{1}{s^2(1 + \frac{m}{\gamma}s)} \right) \quad (6)$$

By using partial fraction

$$X(s) = \frac{K}{\gamma} \left(\frac{1}{s^2} - \frac{m/\gamma}{s} + \frac{m/\gamma}{s + \gamma/m} \right) \quad (7)$$

$$X(s) = \frac{K}{\gamma} \cdot \frac{1}{s^2} - \frac{Km}{\gamma^2} \cdot \frac{1}{s} + \frac{Km}{\gamma} \cdot \frac{1}{s + \gamma/m} \quad (8)$$

By using inverse of Laplacian

$$X(t) = \mathcal{L}^{-1}(X(s)) \quad (9)$$

$$X(t) = \frac{K}{\gamma} t - \frac{Km}{\gamma^2} + \frac{Km}{\gamma^2} \cdot e^{-\frac{\gamma}{m}t} \quad (10)$$

3 Results and Discussions

One of the most important parameter is the optimization of the response time for the proposed model. The response time depends on different parameters according to model equation (10).

After constructing the model and make simulation using MATLAB program, the model shows good stability and response.

It was leading the series of the simulations of the process with changing the values of the injection factor (γ). It can be observed that at $M = 0.005$ Kg, $K = 1.13$ N, and at different values of $\gamma = 500, 1000,$ and 200 N.s/m, by increasing value of gamma it takes more time to reach final value, as shown in Figure 2. Model equation (10) showed that the response time is inversely proportional to the injection factor (γ).

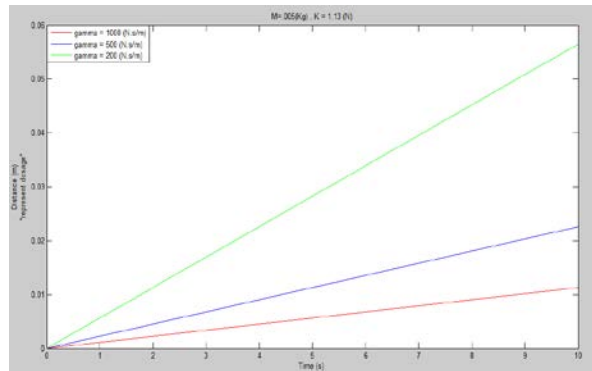


Figure 2. Response time as a function of injection factor (γ).

It was leading the series of the simulations of the process with changing the values of force gain factor (K). It can be observed that at $M = 0.005$ Kg, $\gamma = 300$ N.s/m, and at different values of $K = 0.8, 1.13$ and 2 N, by increasing value of K it takes less time to reach final value, as shown in Figure 3. Also, it can be observed that the model equation (10) showed that the response time is proportional to the force gain factor (K).

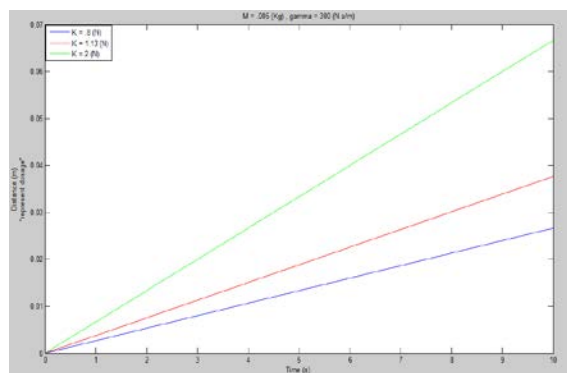


Figure 3. Response time as a function of force gain factor (K).

4 Conclusions

Mathematical model for transportation of medications and drugs through the skin is derivative and described. This model provides a significant reduction of medical complications and improvement in patient compliance. The model shows good stability and response. The response time depends on different parameters according to model equation (10) such as the injection factor (γ) and force gain factor (K). This model is cheap and reliable. The proposed study is simulated by MATLAB program.

The results are demonstrated the proposed study based on a clear procedure. This study is positively led to decrease the patient's pain. In our future works, our study will be used practical experiments.

REFERENCES

- [1] Torin, J.; Sivaloganathan, S.; Kohandel M.; Marianna, F., *Drug delivery through the skin: molecular simulations of barrier lipids to design more effective noninvasive dermal and transdermal delivery systems*

- for *small molecules, biologics, and cosmetics*. John Wiley & Sons, Inc. WIREs Nanomedicine and Nanobiotechnology, 2011. 3: p. 449-462.
- [2] Ahlam, Z.; Maelíosa, T.; Ryan, F., *Transdermal Drug Delivery: Innovative Pharmaceutical Developments Based on Disruption of the Barrier Properties of the stratum corneum*. Pharmaceutics, 2015. 7: p. 438-470.
- [3] Marc, B.; Gary, P.; Stuart, A.; Franklin, K., *Dermal and Transdermal Drug Delivery Systems: Current and Future Prospects*. Drug Delivery, 2006. 13: p. 175-187.
- [4] Adam, C.; Heather, A., *Transdermal and Topical Drug Delivery Principles and Practice*.ed 2012, John Wiley & Sons, Inc.
- [5] Arora, A.; Prausnitz, M.; Mitragotri, S., *Micro-Scale Devices for Transdermal Drug Delivery*. International Journal of Pharmaceutics, 2008. 364: p. 227-236.
- [6] Donnelly, R.; Singh, T.; Garland, M.; Migalska, K.; Majithiya, R.; McCrudden, C.; Kole, P.; Mahmood, T.; McCarthy, H; Woolfson, A., *Hydrogel - Forming Microneedle Arrays for Enhanced Transdermal Drug Delivery*. Adv. Funct. Mater, 2012. 22: p. 4879-4890.
- [7] Torrisi, B.; Tuan, T.; McCrudden, M.; McAlister, E.; Garland, M.; Singh, T.; Donnelly, R., *Microneedles for Intradermal and Transdermal Drug Delivery*. European Journal of Pharmaceutical Sciences, 2013. 50: p. 623-637.
- [8] Anselmo, A.; Mitragotri, S., *An Overview of Clinical and Commercial Impact of Drug Delivery Systems*. J. Control. Release, 2014. 190: p. 15-28.
- [9] Brambilla, D.; Luciani, P.; Leroux, J., *Breakthrough Discoveries in Drug Delivery Technologies: The Next 30 years*. J. Control. Release, 2014. 190: p. 9-14.
- [10] Charman, S.; McLennan, D.; Porter, C, *Subcutaneous Drug Delivery and the Role of the Lymphatics*. Drug Discov. Today Technol., 2005. 2: p. 89-96.
- [11] Park, E.; Dodds, J.; Smith, N., *Dose comparison of ultrasonic transdermal insulin delivery to subcutaneous insulin injection*. Int J Nanomedicine, 2008. 3: p. 335-341.
- [12] Schoellhammer, C.; Blankschtein, D.; Langer, R., *Skin Permeabilization for Transdermal Drug Delivery: Recent Advances and Future Prospects*. Expert Opin. Drug Deliv., 2014. 11: p. 393-407.
- [13] Pillai, O.; Nair, V.; Panchagnula, R., *Transdermal Iontophoresis of Insulin: IV. Influence of Chemical Enhancers*. Int. J. Pharm., 2004. 269: p. 109-120.
- [14] Ajay, K.; Kalluri, H., *Transdermal Delivery of Proteins*. American Association of Pharmaceutical Scientists, PharmSciTech, 2011. 12: p. 431- 441.
- [15] Yunus, A.; John, M., *Fluid Mechanics: Fundamentals and Applications*. ed 2006, McGraw-Hill.
- [16] Prausnitz, M.; Langer, R., *Transdermal drug delivery*. Nature Biotechnology, 2008. 26: p. 1261-1268.

- [17] Schumm, P.; Scoglio, C.; VanderMerwe, D., *A network model of successive partitioning-limited solute diffusion through the stratum corneum*. Journal of Theoretical Biology, 2010. 262: p. 471-477.
- [18] Barry, B.; Harrison, S.; Dugard, P., *Vapour and liquid diffusion of model penetrants through human skin; correlation with thermodynamic activity*. J Pharm Pharmacol, 1985. 37: p. 226-236.
- [19] Kalluri, H.; Banga, A., *Microneedles and transdermal drug delivery*. Journal of Drug Delivery Science and Technology, 2009. 19: p. 303-310.
- [20] Devraj, D.; Mohd, A., *A Review: Different Generation Approaches of Transdermal drug delivery System*. J.Chem. Pharm. Res., 2010. 2: p. 184-193.
- [21] Shinkai, N.; Korenaga, K.; Takizawa, H., *Percutaneous penetration of felbinac after application of transdermal patches: Relationship with pharmacological effects in rats*. J Pharm Pharmacol, 2008. 60: p. 71-76.
- [22] Rje, H.; Jenny, N.; William, M., *Properties of the Glomerular Barrier and Mechanisms of Proteinuria*. Physiol Rev, 2008. 88: p. 451-487.
- [23] Martin, G.; Moss, M.; Wheeler, A.; Mealer, M.; Morris, J.; Bernard, G., *A randomized, controlled trial of furosemide with or without albumin in hypoproteinemic patients with acute lung injury*. Critical Care Medicine, 2005. 33: p. 1681-1687.
- [24] Martin, R.; Susan, E.; Melanie, P.; and Lance, D., *The Glomerulus: The Sphere of Influence*. Clinical Journal of the American Society of Nephrology, 2014. 9: p. 1461-1469.

Automated 3-D Tissue Segmentation via Clustering

S. Edwards, S. Brown, M. Lee

Computational Sciences Division, U.S. Army Research Laboratory, Aberdeen Proving Ground, MD
samuel.edwards@parsons.com; scott.e.brown96.ctr@mail.mil; michael.s.lee131.civ@mail.mil

ABSTRACT

Generation of 3-D tissue models from medical imagery is useful for surgical planning and computer simulations, but often requires some amount of manual effort. In this work, we use the clustering algorithm, DBSCAN, in concert with a 3-D buildup procedure to automatically generate 3-D surface models of the brain and lungs from computed tomography head and chest scans, respectively. Extensions to other tissue types such as heart and liver are demonstrated for contrast-enhanced imagery.

Keywords: medical images, magnetic resonance imaging, computer-assisted tomography, clustering, DBSCAN

1 Introduction

Whole 3-D tissue segmentation is valuable for surgical planning and computer modeling and simulation. Specifically, the military and transportation sectors are interested in simulating the effects of various external trauma to hard and soft tissue [1]. Accurate models of organs from various individuals can improve the fidelity of these simulations. However, 3-D image segmentation can often involve a significant amount of tedious manual effort. We strive to automate this process for the convenient extraction of 3-D tissue models from stacked sets of computed tomography (CT) scans. While magnetic resonance imaging (MRI) may yield more detailed models, this modality is not suitable for individuals that may have metallic elements within their body, which could likely result from traumatic events.

Density-based spatial clustering of applications with noise [2], or DBSCAN, has become a popular tool for image segmentation due to its ability to 1) detect segments of arbitrary shape 2) and not require *a priori* specification of the number of segments to extract. These desirable features allow DBSCAN to be applied to a series of images with only determination of a single set of parameters. In the case of medical imagery, DBSCAN has been mostly used in the context of tumor segmentation. Remarkably versatile, DBSCAN can precisely segment lesions from images of skin [3] and tumors from a brain MRI [4]. Additionally, enhanced versions of DBSCAN properly extract lung nodules from CT scans [5].

Other algorithms have demonstrated promising results in medical image segmentation. The watershed algorithm [6] has been adapted to segmenting medical imagery. The algorithm can detect lung lesions from CT scans [7], much like the application of DBSCAN in this similar problem [5]. However, unlike the watershed approach, DBSCAN is more sensitive to the gray values of individual segments, allowing more

elaborate segmentation. Seeded region growth [8] is another popular method for medical image segmentation. There even exist fully automated versions of this algorithm specifically for medical imaging [9]. However, the method of region growing is limited to the segmentation of one tissue at a time. Since DBSCAN clusters the entire image, it is a more practical choice.

The construction of accurate patient-specific 3-D tissue models from medical scans has the potential to revolutionize surgical planning [10]; procedures already exist to optimize the 3-D printing of these models [11]. Historically, 3-D tissue segmentation is conducted manually [12] using tools such as 3DSlicer [13] and MIMICS 19.0 [14]. Recent advances in segmentation software have made semi-automatic approaches to segmenting medical images more accessible. However, there is a scarcity of fully automated procedures. The segmentation in these fully automated approaches is conducted either statistically or by simple thresholding depending on the desired tissue. For example, the liver is large in comparison to other organs in the abdomen and has a homogeneous intensity in medical images, allowing it to be extracted by statistically analyzing regions in the scan [15]. Furthermore, bone typically has a much higher intensity in medical imagery than other anatomical structures and can therefore be extracted by thresholding out other soft tissue [16]. The actual construction of the models can be handled through interpolation between stacked slices [16] or through minimizing a cost function [17].

In this work, we revisit the possibility of automated 3-D tissue segmentation. General realization of this goal for all tissue types would require human-level skill in the interpretation of medical imagery. Instead, we present a cluster-based segmentation algorithm that utilizes DBSCAN and a novel stacking algorithm to construct 3-D models of tissue.

2 Theory

2.1 DBSCAN

Unlike many other clustering algorithms, DBSCAN measures distance in terms of graph connectivity rather than a simple Euclidean metric, meaning that detected segments can deviate far from circularity. We briefly outline the method here. Define the ϵ -neighborhood of a point p to be the set of points that are at most ϵ from p . We call p a *core point* if its ϵ -neighborhood contains at least m points. A point q is ϵ -reachable from p if there exists a path of points $p_1 = p, p_2, \dots, p_n = q$ such that p_i is a core point and its ϵ -neighborhood contains p_{i+1} for all $1 \leq i \leq n-1$. A cluster is the maximal set of points ϵ -reachable from a core point p . Points that are not reachable from any core point are labeled as noise.

2.2 Image Segmentation via DBSCAN

Ye et al. [18] was one of the first groups to show that clustering algorithms, especially DBSCAN, can be used to segment images. Consider that each pixel p_i of a CT scan image has coordinates (x_i, y_i) and a gray value c_i . Given that we desire to cluster pixels by both spatial proximity and value, we treat each pixel as a 3-dimensional point, where the value becomes the third coordinate, ranging from 0 (black) to 255 (white). In DBSCAN terminology, a pixel, p_j , with coordinates (x_j, y_j) and value c_j , is ϵ -reachable from p_i if

$$(x_j - x_i)^2 + (y_j - y_i)^2 + \alpha(c_j - c_i)^2 < \epsilon$$

where the arbitrary scale factor α acknowledges that the dimensional units of location and value are incommensurate. For this work, we set α to 1, because the height and width of typical CT scans are within an order of magnitude of the value range (256).

2.3 3-D Voxel Segmentation

Typically, 3-D tissue models can be derived by stacking 2-D medical scans [16]. For this work, we developed an algorithm to merge segments from 2-D DBSCAN segmentations resulting in multiple 3-D voxel segments, which are then converted into surfaces. The procedure begins with identifying unique segments $S_{a,1}$ (where a is the segment index) in the top scan in a given direction (e.g., axial). The second scan is then compared with the first, where each segment $S_{b,2}$ is relabeled to account for matches with the first scan. When a segment $S_{b,2}$ shares some of the same pixel locations with $S_{a,1}$, and has at least N corresponding pixel values that no more than τ apart in gray value, then that segment is relabeled to index of the segment from the first scan. If there is more than one common segment from the first scan for a given $S_{b,2}$, the one with the most pixels in common "wins." If a segment $S_{b,2}$ has no first scan counterparts, it is given a new index, incremented from all previous unique labels. This procedure is repeated for all scans, sequentially looping through adjacent scans. Then, the process is repeated starting backwards from the bottom scan, to merge segments that started off as two or more fragments from the top but, at some point, should have merged into one complete segment. With the series of 2-D segments now having been given common labels, they are merged into an individual voxel array per each unique label, and each voxel array is converted to a surface using the marching cubes algorithm [19]. For now, the generated surfaces must be manually selected for the wanted tissue type, but a fairly simple heuristic is that the larger surfaces tend to be the desired outputs.

3 Methods

3.1 Databases

Medical imagery, all in DICOM format, was downloaded from three separate databases. The first two databases were obtained from the Cancer Imaging Archive [20]. The Head-Neck Cetuximab study documents patients with stage III and IV head and neck cancer before and after treatment with the epidermal growth factor receptor (EGFR) inhibitor Cetuximab [21]. From this repository, we obtained three full body series that were utilized for brain extraction. The second database from this archive, named LungCT-Diagnosis, contained series of scans with a slice thickness between three to six millimeters that were taken for diagnosis prior to surgery [22]. These images were enhanced with a contrast medium, allowing the heart and liver to be segmented in addition to the lungs. The final database was the result of a collaboration between the ELCAP and VIA research groups to create a dataset for detection software [23]. It consists of series of unenhanced chest CT scans possessing a slice thickness of 1.25 mm. Without the contrast medium, only the lungs were extracted from this last database. We leave it as future work to determine the process to extract 3-D models of the heart and liver from unenhanced scans.

3.2 Procedure

3.2.1 Preprocessing

The DICOM files are first read into our program using VTK tools [24]. CT scans reflect the radiodensity of tissue measured in Hounsfield units (HU) [25]. Air and water at standard temperature and pressure have defined radiodensity values of -1000 and 0 HU respectively. A preliminary thresholding is applied to highlight certain desired tissue and therefore refine the segmentation process. The image is then converted from HU to grayscale by simply scaling the data. To remove extraneous noise while retaining edge integrity, two passes of bilateral filtering [26] are applied to the images.

3.2.2 Segmentation

Before clustering in bulk, we first establish the values for DBSCAN parameters to best extract different tissue types. We define the minimum number of points needed in the declaration of a core point m to be some fraction f of the area of the ϵ -neighborhood — that is,

$$m = f\pi\epsilon^2.$$

The circular assumption of nearby points can be used since the pixels of an image are, by definition, densely packed on a square lattice. With fractions $f < 1$, regions with sharp, non-circular edges can be detected. Experimentation with ϵ , f , and thresholding values was conducted to determine sufficient values for each tissue type, as seen in Table 1.

Table 1: The values of ϵ , the fraction of the area of the ϵ -neighborhood f , and the thresholding values in HU that were determined to be suitable for DBSCAN-based segmentation of each tissue type.

Tissue Type	ϵ	f	Min	Max
Brain	4	0.1	-50	200
Lung	8	0.3	-800	-300
Heart (contrasted)	4	0.2	-50	200
Liver (contrasted)	6	0.4	-50	200

3.2.3 3-D Construction

The buildup portion of our algorithm requires two additional parameters when determining whether to merge two segments from different slices: the number N of corresponding pixel locations between two segments whose values must be no more than τ apart. Through experimentation, we determined the values of $N = 50$ and $\tau = 20$ produced a clean result with the high resolving power of smaller structures.

3.3 Software

All the algorithms for this work were written in Python, using various common add-on modules. Scikit-image was used to process images and Scikit-learn was used to perform DBSCAN clustering [27]. Besides initial DICOM reading, the VTK toolkit [24] was also used to create the 3-D models. The standard-format triangulated-surface STL files were rendered in Paraview [28]; the inclusion of OSPRay [29] enhanced surface display by adding ambient occlusion and shadows.

4 Results and Discussion

4.1 The 2-D Case

We experimented with different clustering algorithms that did not require the number of clusters to be specified as a parameter. The watershed method simply outlines regions, impeding the reliance of the buildup algorithm on merging filled segments together; therefore, it was disregarded. We also ruled out the region growing method because of its inability to simultaneously segment more than one region from the image. Ultimately, we narrowed our search to DBSCAN and mean shift, an algorithm that computes clusters by finding modes of the underlying probability density function of the data [30].

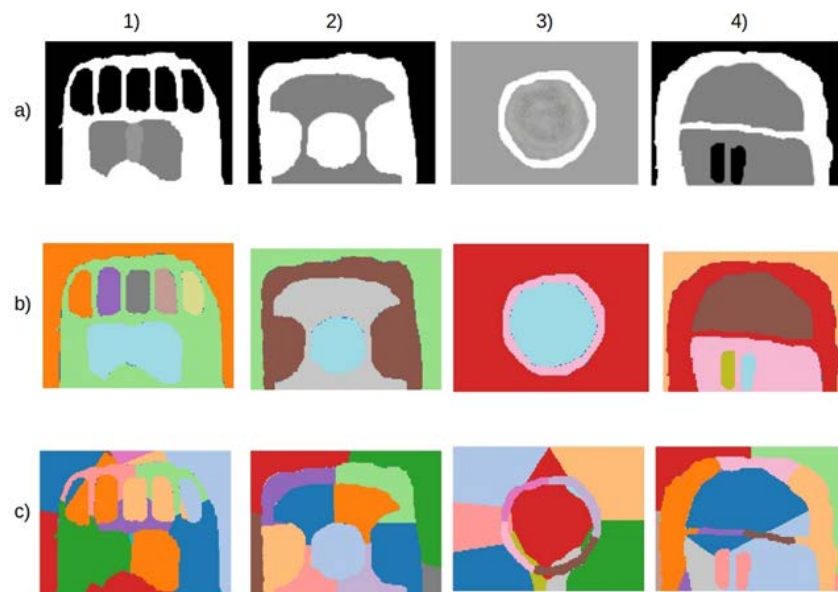


Figure 1: The toy images (a) and the results of applying DBSCAN (b) with $\epsilon = 4$ and $f = 0.2$ and mean shift (c).

By constructing toy models that mimicked various features of the skull, such as a thin border between two similarly colored regions, we determined that DBSCAN would operate more effectively on medical images. Notice that for every case in Figure 1, mean shift creates more clusters than necessary by segmenting large regions of homogeneous color, a disconcerting feature for a segmentation algorithm. On the other hand, DBSCAN accurately segments each image, even ignoring the abundance of noise present in image (a3).

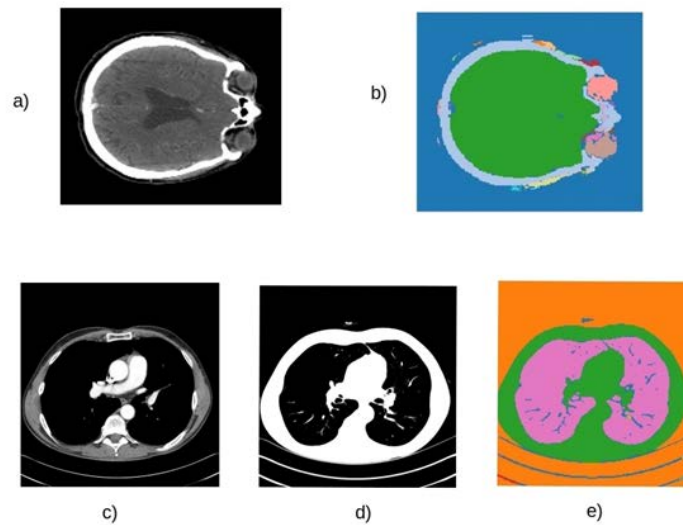


Figure 2: A CT scan of a human skull (a) and chest cavity (c) and the resulting segmentation by DBSCAN (b) and (e) respectively, using the parameters from Table 1. The thresholded chest cavity (d) is included to emphasize the bronchial tubes that are masked in the original image.

4.2 3-D Models

4.2.1 Bone

Segmenting bone from CT scans may be done trivially through simple thresholding as its values are typically higher than that of surrounding tissue. However, utilizing the same parameters as the brain ($\epsilon = 4$ and $f = 0.1$), our algorithm can provide a more precise segmentation of bone than that from thresholding.

Thresholding is less effective for several reasons. Foreign objects such as metals register very highly on the Hounsfield scale; therefore, they are captured by the thresholding, as evidenced by the inclusion of the bed frame in row (b) of Figure 3. Additionally, various bone types yield different Hounsfield values. For example, the skull bones have a much higher value than that of the ribs. Notice in row (b) of Figure 3 that the skull is well-defined, but the clavicle, ribs, and sternum are severely lacking. Although our algorithm separates the skeleton into three clusters in this case, it provides much more detail globally and does not include any extraneous materials, such as the metal bed frame.



Figure 3: The results of segmentation of the skeleton of patient 0013 of the Head-Neck Cetuximab study [21] by our algorithm (a) and thresholding (b) respectively. Our algorithm segmented the skeleton into three separate regions, reflected by the different colors.

4.2.2 Brain

Segmenting the brain yields some of the most promising and repeatable results from this algorithm, likely because the brain is surrounded by the skull, providing a clear separation from other soft tissue. It is even possible to cluster the brain and spinal cord together, as evidenced by Figure 4. However, this feature does not appear in brain models segmented from full body scans. The intricate creasing present on the back of the brain and the detailed cerebellum exemplify the power of this algorithm. The folding pattern of the brain is unable to be detected both because of the loss of detail in the CT scans and the necessary application of bilateral filtering [24].



Figure 4: The segmented brain from patient 0013 from the Head-Neck Cetuximab study [21].

The brain models appearing in Figure 5 are taken from full body scans. The lack of attachment to the spinal cord is likely because the spinal cord is typically clustered with back muscles in lower torso scans or sometimes missed altogether. While the parameters for the segmentation are more attuned to the brain segmented in Figure 4, the fact that detailed brain models can be extracted from other patients demonstrates the reproducibility of the algorithm.

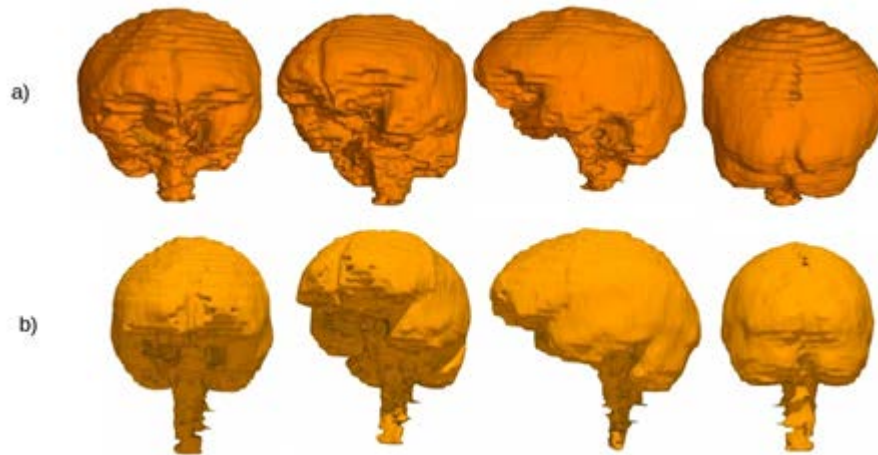


Figure 5: The segmented brains from patient 0001 (a) and 0009 (b) from the Head-Neck Cetuximab study [21].

4.2.3 Lungs

The lungs stand out in stark contrast with the rest of the soft tissue in the body because of the air contained within them. There is a simple way to segment the lungs by extracting their imprint; however, this method is impractical, as it ignores the bronchial tubes. The ideal lung segmentation should include some details of the bronchial tubes and a clear majority of the lung tissue.



Figure 6: Segmentation results of the lungs of patient R0006 of the LungsCT-Diagnosis study [22].

Our protocol can not only depict the shape of the outer lung but discern a great amount of detail from the bronchial tubes as well, as illustrated by Figure 6. This trend seems to be reproducible as well. When applied to all fifty lungs in the ELCAP-VIA database, our algorithm performed quite well by accurately segmenting most of the lungs; this data is included in the supplementary materials.

4.2.4 Other Tissue

Our protocol has shown promising results for extracting other tissue types. It could segment the heart and liver in scans enhanced with contrast medium as seen in Figs. 7 and 8. However, the algorithm failed when the same parameters were applied to uncontrasted scans. In the uncontrasted case, the gray values of the heart closely resemble those of the chest muscles; similarly, it is difficult to discern the liver from the surrounding abdominal tissue.

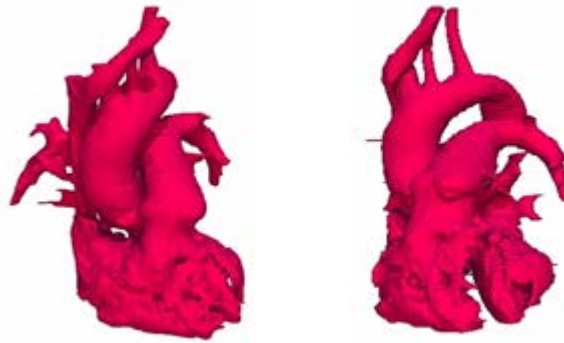


Figure 7: Segmentation results of a contrasted heart of patient R0006 of the LungsCT-Diagnosis study [22].

The segmentation displays a detailed contouring of the aorta and pulmonary artery. Even the superior vena cava is intricately defined. However, apparent gaps exist on the body of the heart and no chamber information can be discerned when the surface is made partially transparent.

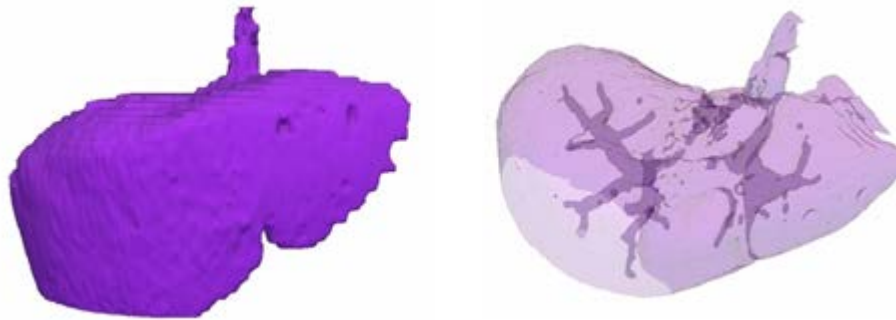


Figure 8: Segmentation results of a contrasted liver of patient R0006 of the LungsCT-Diagnosis study [22].

Our approach is able to properly capture some extent of the hepatic ducts, although it was unable to detect the ligament that splits the liver.

Segmenting muscle tissue has proven to be particularly challenging. The segments are typically in many pieces and lacking large chunks of tissue. One likely explanation is the variability of muscle shape throughout the body is not conducive for a global set of parameters. Additionally, muscle tissue is very similar in appearance to other soft tissue in the body which could disrupt segmentation.

4.3 Limitations

Although our procedure provides a convenient and efficient method for 3-D segmentation, it is by no means a perfect solution to the problem. Certain unavoidable phenomenon in the scans themselves could result in undesirable outcomes. The CT scans often yield a circular working image; a black background fills the remainder of the square frame. In off-center scans, the lungs may be clustered with this black background by DBSCAN, as in Figure 9. However, this problem may be remedied by either cropping the image so that only the circular scan is processed or by setting the black background to white.

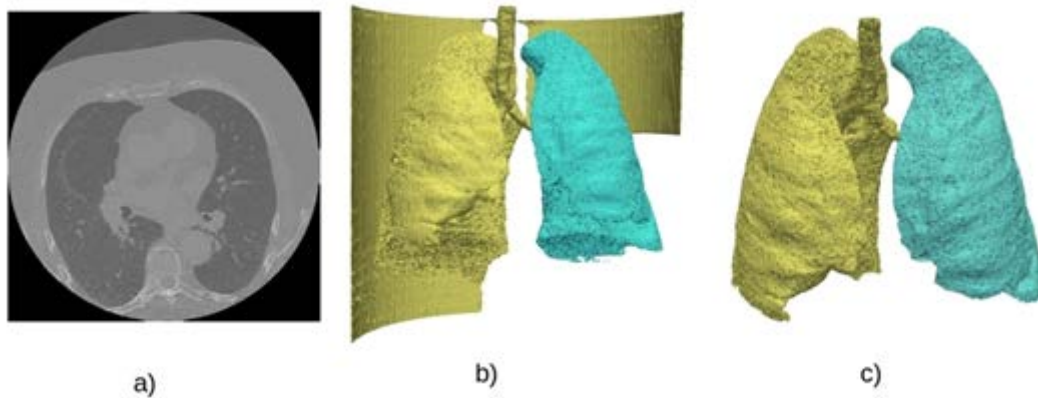


Figure 9: Depicting the impact of off-center CT scans from patient W0008 in the ELCAP-VIA database [23]. The sample scan (a) and the results of the segmentation algorithm if run normally (b). By setting the outer region of the scan from black to white, the segmentation results were much more accurate (c). The colors in (b) and (c) represent the different segments detected.

Another obstruction to clean segmentation is the presence of concentrated dyes or foreign objects with a high radiodensity such as metals. This creates a bright spot that extends outwards in a gradient, disrupting our algorithm. Since we view color as a third dimension, the gradient creates a ramp, possibly causing points from two separate regions to be ϵ -reachable. In the case of patient W0014 depicted in Figure 10, the lungs in this slice were merged with the background, creating a region that exceeded our threshold of pixel size for segments. Therefore, the top quarter of the left lung was unable to be detected by our algorithm. If we had decreased ϵ to incorporate this region, then the entire background would have been included in the segmentation, masking the lungs.

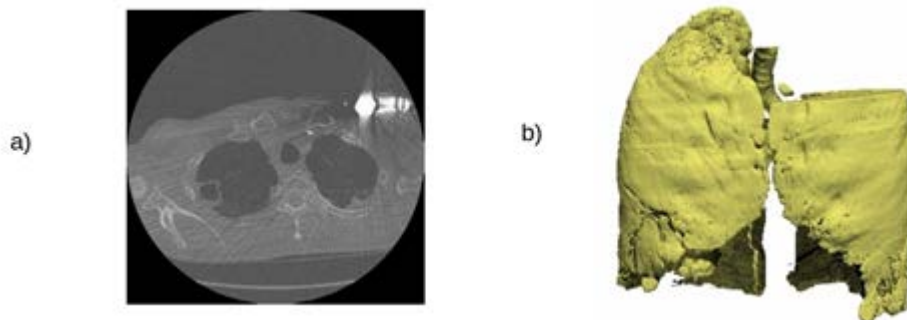


Figure 10: The sample scan (a) and the results of the segmentation algorithm (b) that depict the impact of a bright spot from patient W0014 in the ELCAP-VIA database [23].

Finally, widespread noise can be detrimental to the segmentation, as seen acutely for the detailed extraction of bronchial tubes. While an abundance of noise seems to be almost negligible for the segmentation of soft tissue of homogeneous density like the brain and liver, it can profoundly impact the segmentation of lung tissue.

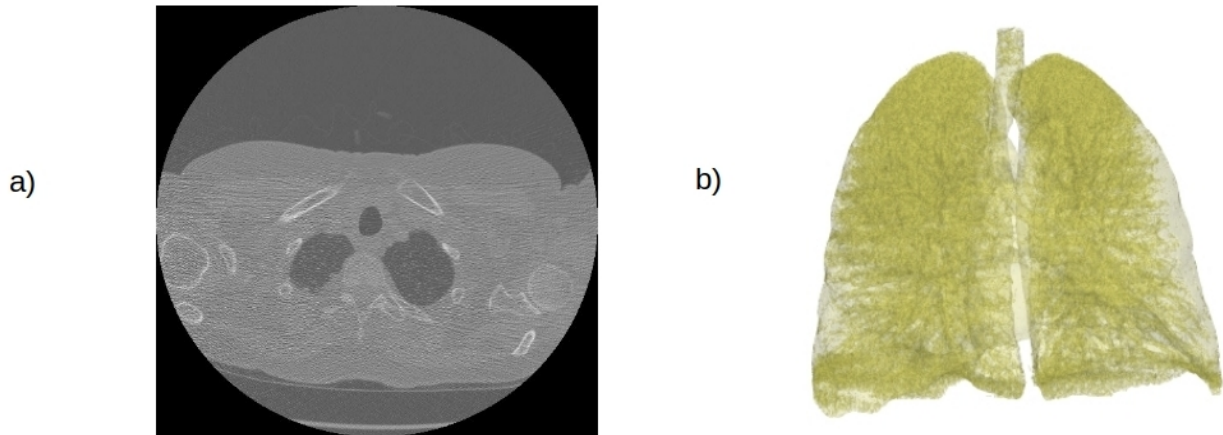


Figure 11: The results of a noisy scan on patient W0007 in the ELCAP-VIA database [23]. The sample scan (a) and the results of the segmentation algorithm (b).

Notice the white speckles present over the lung tissue in image (a) of Figure 11. DBSCAN will not cluster this noise with the lung tissue; therefore, very little detail from the bronchial tubes can be detected. Furthermore, intense noise can cause the inside of the lungs to appear spongy, which not only masks the inside of the lungs but could lead to a misdiagnosis as well, if these models were used in a clinical context.

5 Conclusion

Automated 3-D segmentation of various tissue types could impact surgical planning, medical training, diagnosing patients, and simulation from real tissue models. Although a robust universal solution will likely require more sophisticated approaches, we have developed a simple-to-use protocol for fully automated 3-D segmentation of certain tissue types. This algorithm does possess a few limitations, but its ability to accurately segment multiple organs demonstrates its versatility. We present a method to extract the heart and liver from scans enhanced with contrast medium; extending the results to unenhanced scans is reserved for future work. Furthermore, extending this work to MRI may yield more detailed results for certain tissue types where CT scans have limited resolving power.

REFERENCES

- [1]. A. N. Ranslow, et al., *Microstructural analysis of porcine skull bone subjected to impact loading*. ASME 2015 International Mechanical Engineering Congress and Exposition, American Society of Mechanical Engineers, 2015.

- [2]. M. Ester, et al., *A density-based algorithm for discovering clusters in large spatial databases with noise*. Kdd, Vol. 96, 1996, pp. 226–231.
- [3]. M. E. Celebi, Y. A. Aslandogan, P. R. Bergstresser, *Mining biomedical images with density-based clustering*. Information Technology: Coding and Computing, 2005. ITCC 2005. International Conference on, Vol. 1, IEEE, 2005, pp. 163–168.
- [4]. S. K. Bandyopadhyay, T. U. Paul, *Segmentation of brain tumour from mri image analysis of k-means and dbscan clustering*. International Journal of Research in Engineering and Science 1 (1) (2013) 48–57.
- [5]. W. Zhang, X. Zhang, J. Zhao, Y. Qiang, Q. Tian, X. Tang, *A segmentation method for lung nodule image sequences based on superpixels and density-based spatial clustering of applications with noise*. PloS one 12 (9).
- [6]. L. Vincent, P. Soille, *Watersheds in digital spaces: an efficient algorithm based on immersion simulations*. IEEE Transactions on Pattern Analysis & Machine Intelligence (6) (1991) 583–598.
- [7]. Y. Tan, L. H. Schwartz, B. Zhao, *Segmentation of lung lesions on ct scans using watershed, active contours, and markov random field*. Medical physics 40 (4).
- [8]. R. Adams, L. Bischof, *Seeded region growing*. IEEE Transactions on pattern analysis and machine intelligence 16 (6) (1994) 641–647.
- [9]. R. Pohle, K. D. Toennies, *Segmentation of medical images using adaptive region growing*. Proc. SPIE Medical Imaging, Vol. 4322, 2001, pp. 1337–1346.
- [10]. N. J. Mankovich, D. Samson, W. Pratt, D. Lew, J. Beumer 3rd, *Surgical planning using three-dimensional imaging and computer modeling*. Otolaryngologic Clinics of North America 27 (5) (1994) 875–889.
- [11]. T. M. Bücking, E. R. Hill, J. L. Robertson, E. Maneas, A. A. Plumb, D. I. Nikitichev, *From medical imaging data to 3d printed anatomical models*. PloS one 12 (5).
- [12]. K. H. Höhne, W. A. Hanson, *Interactive 3d segmentation of mri and ct volumes using morphological operations*. Journal of computer assisted tomography 16 (2) (1992) 285–294.
- [13]. A. Fedorov, et al., *3d slicer as an image computing platform for the quantitative imaging network*. Magnetic resonance imaging 30 (9) (2012) 1323–1341.
- [14]. Materialise, Mimics software, <http://www.materialise.com> (2016).
- [15]. L. Massoptier, S. Casciaro, *A new fully automatic and robust algorithm for fast segmentation of liver tissue and tumors from ct scans*. European radiology 18 (8) (2008) 1658.
- [16]. K. Subburaj, B. Ravi, *High resolution medical models and geometric reasoning starting from ct/mri images*. 10th IEEE International Conference on Computer-Aided Design and Computer Graphics, IEEE, 2007, pp. 441–444.

- [17]. T. Heimann, I. Wolf, H.-P. Meinzer, *Active shape models for a fully automated 3d segmentation of the liver—an evaluation on clinical data*. Medical Image Computing and Computer-Assisted Intervention—MICCAI 2006 (2006) 41–48.
- [18]. Q. Ye, W. Gao, W. Zeng, *Color image segmentation using density-based clustering*. Multimedia and Expo, 2003. ICME'03. Proceedings. 2003 International Conference on, Vol. 2, IEEE, 2003, pp. II–401.
- [19]. W. E. Lorensen, H. E. Cline, *Marching cubes: A high resolution 3d surface construction algorithm*. ACM siggraph computer graphics, Vol. 21, ACM, 1987, pp. 163–169.
- [20]. K. Clark, et al., *The cancer imaging archive (TCIA): maintaining and operating a public information repository*. Journal of digital imaging 26 (6) (2013) 1045–1057.
- [21]. W. R. Bosch, W. L. Straube, J. W. Matthews, J. A. Purdy, *Data from head-neck cetuximab*. Tech. rep., The Cancer Imaging Archive (2015).
- [22]. O. Grove, et al., *Quantitative computed tomographic descriptors associate tumor shape complexity and intratumor heterogeneity with prognosis in lung adenocarcinoma*. PloS one 10 (3) (2015) e0118261.
- [23]. A. P. Reeves, Y. Xie, S. Liu, *Large-scale image region documentation for fully automated image biomarker algorithm development and evaluation*. Journal of Medical Imaging 4 (2) (2017) 024505–024505.
- [24]. W. J. Schroeder, B. Lorensen, K. Martin, *The visualization toolkit: an object-oriented approach to 3D graphics*, Kitware, 2004.
- [25]. G. N. Hounsfield, *Computerized transverse axial scanning (tomography): Part 1. Description of system*. The British journal of radiology 46 (552) (1973) 1016–1022.
- [26]. C. Tomasi, R. Manduchi, *Bilateral filtering for gray and color images*. Computer Vision, 1998. Sixth International Conference on, IEEE, 1998, pp. 839–846.
- [27]. E. Jones, et al., *SciPy: Open source scientific tools for Python* (2001). URL <http://www.scipy.org/>
- [28]. J. Ahrens, B. Geveci, C. Law, *Paraview: An end-user tool for large data visualization*, The Visualization Handbook 717.
- [29]. I. Wald, G. P. Johnson, J. Amstutz, C. Brownlee, A. Knoll, J. Jeffers, J. Günther, P. Navratil, *Ospray—a cpu ray tracing framework for scientific visualization*. IEEE transactions on visualization and computer graphics 23 (1) (2017) 931–940.
- [30]. D. Comaniciu, P. Meer, *Mean shift: A robust approach toward feature space analysis*. IEEE Transactions on pattern analysis and machine intelligence 24 (5) (2002) 603–619.

Calculation of Inversion Time (TI) value for Fat Suppression in the Modified Spin Echo Sequence Method.

¹Sunil Kalagi

¹BioMedical Physics, School of Medical Sciences, University of Aberdeen, Foresterhill, Aberdeen, UK
sunilkalagi@gmail.com

ABSTRACT

Fat suppression is commonly used in Magnetic Resonance Imaging (MRI) to suppress the signal from adipose tissue or detect adipose tissue. Due to short relaxation times, fat has a high signal on magnetic resonance images (MRI). This high signal, easily recognized on MRI. The high signal due to fat may be responsible for artifacts such as ghosting and chemical shift. Lastly, a contrast enhancing tumor may be hidden by the surrounding fat. These problems have prompted development of fat suppression techniques. in MRI. Fat may be suppressed on the basis of its difference in resonance frequency with water by means of frequency selective pulses or phase contrast techniques, or on the basis of its short T1 relaxation time by means of inversion recovery sequences. The aim of this paper is to study the Fat suppression technique using Inversion recovery Pulse sequence by calculating T_{1null} parameter for the pulse sequence.

Keywords: Fat Suppression; Inversion Time; Spin Echo Sequence.

1 Introduction

In MRI fat suppression is essential for accurate diagnosis which may obscure underlying pathology. [1-6] The different chemical environments of fat and water cause fat to precess at a lower resonant frequency than water. At 4.7T fat precesses at about 700 Hz less than water.[7-8] This is usually expressed as -3.5 parts per million of the main field strength. [8-9]

A magnetic field gradient allows the resonant frequency of an object to be mapped to its position along the gradient direction [10-12]. Therefore differences in resonant frequency result in differences in position. This results in fat being shifted relative to water in an image and is called the chemical shift artefact δ . [13-15] This is described in terms of frequency as follows

$$\delta = (\Delta f / f_0) 10^6 \quad (1)$$

where Δf = change in frequency (Hz) and f_0 = Centre frequency (Hz). In images this shift is characterised by a dark edge between the fat and water [1,8 and 13].

In situations where the chemical shift artefact is present the fat signal can obscure the water signal from underlying tissue. Here the aim was to find the appropriate value of the inversion time (TI), for use in the modified spin echo sequence, which would suppress the contribution from the fat.[13-15]

DOI: 10.14738/jbemi.52.4323

Publication Date: 10th April 2018

URL: <http://dx.doi.org/10.14738/jbemi.52.4323>

Inversion recovery pulse sequence: Inversion recovery (IR) is a conventional spin echo (SE) sequence preceded by a 180° inverting pulse. In other words, if a SE sequence is denoted by $(90^\circ - 180^\circ\text{-echo})$, the IR sequence can be written as $180^\circ\text{-}(90^\circ\text{-}180^\circ\text{-echo})$. [1-8]

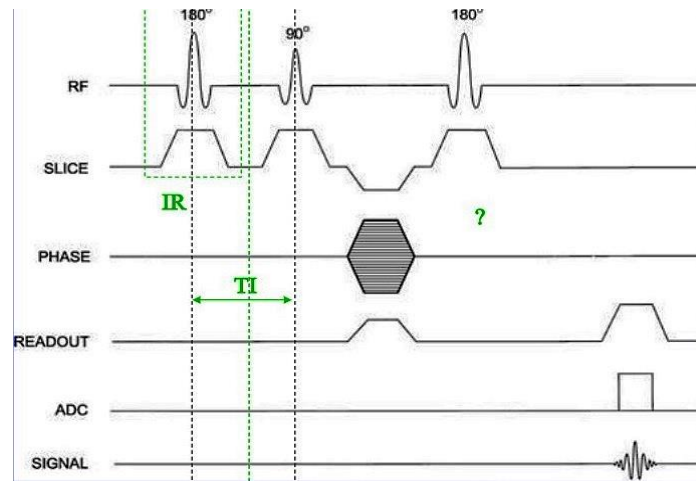


Figure 1. Inversion Recovery (IR) pulse sequence.

The time between the 180° inverting pulse and the 90° pulse is called the inversion time (TI). The repetition time (TR) and echo time (TE) are defined as they are for spin echo. [1-8]

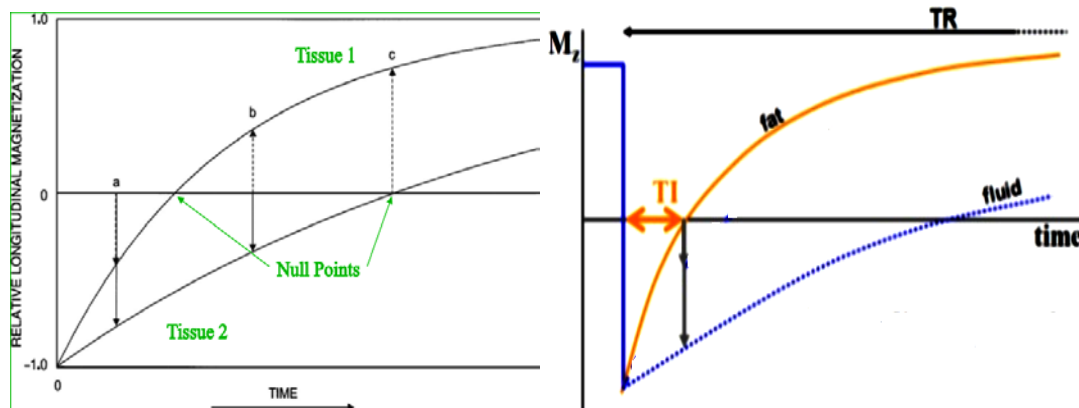


Figure 2 (a) Contrast of Fat(Tissue1) and Water (Tissue2)tissues (b) TI for fat suppression

2 Method

2.1 MRI System:

The Preclinical 4.7 Tesla micro MRI system(Surrey Medical Imaging Systems, UK) located at Biomedical physics department of University Aberdeen was used for our research project. The system consisted of: Magnex 4.7 Tesla superconducting magnet; MR Solutions console and pulse programmer; Magnex shielded gradient coils with Techron drivers capable of producing field gradients of 90mT/m with rise times of 200 μs and Morris Instruments birdcage transmit/receive coil, and other RF coils of in-house design.



Figure 3. The Preclinical 4.7 Tesla micro MRI system with console at University of Aberdeen.

2.2 Sample

A set of 7 tubes containing either water or vegetable oil were imaged together. In order to reduce the relaxation time the water had been doped with copper sulphate. Without fat suppression images were made using the standard spin echo sequence. Two images were obtained in this way – one with an image bandwidth of 25 kHz and the other with 12.5 kHz. The other parameters associated with these images are as follows: Field – of view = 100mm, Slice thickness = 5mm, Echo time (TE) = 40ms and the time between 90° pulses (TR) = 1000ms.

To achieve fat suppression it was necessary to employ an inversion recovery pulse sequence. This pulse sequence includes a 180° pulse to invert the spins onto the negative z– axis. Following this the magnetisation vector slowly returns up the z– axis towards equilibrium. This is due to spin – lattice (T₁) relaxation. When a 90° pulse is applied before equilibrium is reached the magnetisation is transferred from the z – axis to the x-y plane. Spin – spin (T₂) relaxation results in the free induction signal (FIS).

The time between the 180° and 90° pulses is the inversion time (TI). If TI coincides with the time at which the longitudinal magnetisation M_z of the fat is zero then there is no magnetisation from fat to be transferred to the x – y plane. Therefore there is zero contribution of the fat spins to the FIS. This value of TI is referred to as T_{1NULL} and its relationship to T₁ is given below. As the fat and water have different values of T₁ the water will still contribute to the FIS. [1, 2, 3]

$$M_z = M_0(1 - 2\exp(-TI/T_1)) = 0 \quad (2)$$

$$\therefore T_{1NULL} = 0.693T_{1(\text{water/fat})} \quad (3)$$

To obtain an image in which the signals from the tubes of fat are suppressed this value of T_{1NULL} for fat was used in a modified spin echo pulse sequence given below.

$$[180^\circ - TI - 90^\circ - TE/2 - 180^\circ - TE/2 - \text{signal} - TR -]^n \quad (4)$$

This is the spin echo pulse sequence with an additional inversion pulse prior to the start of the spin echo sequence. Here n = 256.

The main field was generated by a 4.7T superconducting solenoid. The RF coil's impedance at resonance was matched to the standard 50Ω output/input impedance of RF power amplifiers/preamplifiers to

ensure efficient transfer from the coil. Shimming was carried out to correct for inhomogeneities in the magnetic field.

3 Results and Discussion

3.1 Without Fat Suppression

The images obtained using the spin echo pulse sequence (without fat suppression) were reconstructed using a contrast factor of 0.05 and are shown below.

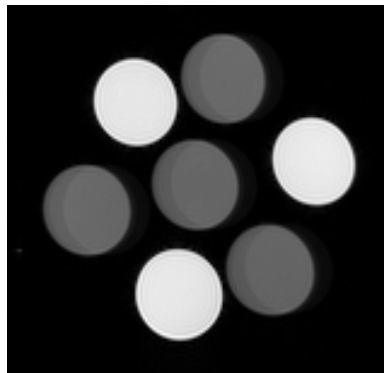


Figure 4. Spin echo image obtained using a bandwidth of 25 kHz

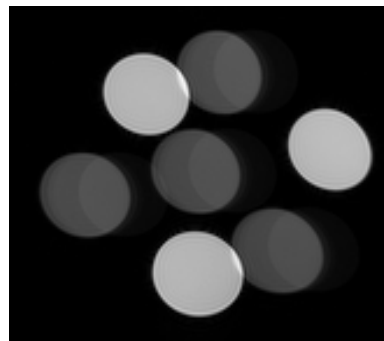


Figure 5. Spin echo image obtained using a bandwidth of 12.5 kHz

At higher field strengths ($>0.5T$) there is known to be a significant shift in fat relative to water. By comparing the images obtained at 25 and 12.5 kHz it was therefore concluded that the bright circles correspond to water and the dark circles to fat. The images show that in addition to being shifted the dark circles are slightly distorted. Also there is a faint circle in *figure 5* in the same position as the fat peak in *figure 4*. This corresponds to the fat also containing some water. The observed shifts of the fat in *figure 5* are quantified in the following section.

(1.1) Chemical shift artefact

The shift of the fat peak in *figure 5* relative to its position in the higher frequency image was found by measuring the distance from the left hand edge of the faint water circle still present in *figure 5* (position x_1) to the left hand edge of the shifted fat circle (position x_2) (see *figure 6*).

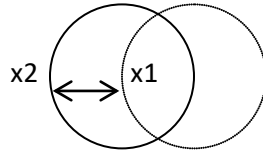


Figure 6. Diagram showing the positions on the fat circles of figure 5 used to calculate the shift of the fat in the 12.5 kHz image relative to its position in the 25 kHz image.

The values used to measure the shift of the 4 fat samples in figure 5 are as follows

Table 1. Values of positions on the fat circles in figure 5 used to calculate the shift (Δx) of fat relative to water in millimetres (mm).

x1(mm)	x2(mm)	Δx (mm)
-24.6	-30.9	-6.3
-6.3	-12.1	-5.8
-7.8	-1.6	-6.2
-1.6	-7.8	-6.2

In figure 5 the bandwidth is 12.5 kHz and the centre frequency (f_0) is 199.9 MHz. Since the field of view is 100mm \times 100mm, 1mm corresponds to 125 Hz. This allows the shift in millimetres (Δx) to be converted to a shift in frequency (Δf). Using these values and the centre frequency ($f_0 = 199.1\text{MHz}$) the chemical shift (δ) can be calculated according to equation 1. These values are given in Table 2 and are close to the expected shift of fat relative to water (-3.5ppm) .

Table 2. chemical shift values δ corresponding to the fat samples in figure 5 calculated according to equation 1 using change in frequency Δf .

Δx (mm)	Δf (Hz)	δ (ppm)
-6.3	-787.5	-3.94
-5.8	-725	-3.64
-6.2	-775	-3.89
-6.2	-775	-3.89

(1.2) $T_{I_{NULL}}$ and T_1

Using the inversion recovery pulse sequence the $T_{I_{NULL}}$ value was estimated by suppressing the fat peak of the Free Induction Signal (FIS). By trial and error this was found to be 140ms. From this T_1 was calculated according to equation 3 and was found to be 201.6ms.

3.2 With Fat Suppression

The image below was obtained by including the estimated value of $T_{I_{NULL}}$ for fat (140ms) in the modified spin echo pulse sequence (see theory section). It was reconstructed using a contrast factor of 0.2.

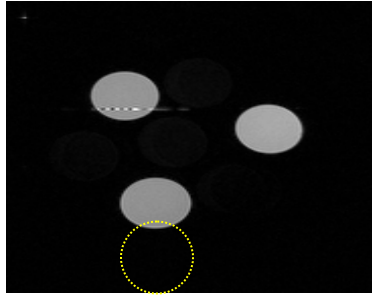


Figure 7. Fat suppression achieved using the modified spin echo sequence with $T_{I\text{NULL}}$ and a bandwidth of 25 kHz. The yellow circle represents the approximate region of the fat sample in figure 4.

3.3 Quantifying Fat suppression

3.3.1 Visual inspection

That only the brighter circles remain indicates that fat suppression has been successful. However the circles corresponding to the water samples look darker than in previous images. The line across the top left hand side water sample is an artefact caused by the imager.

3.3.2 Fat to Water Ratio

To formally quantify fat suppression it is necessary to compare the fat to water signal intensity with (*figure 7*) and without (*figure 4*) fat suppression. For this comparison the water sample at the bottom of *figures 4 and 7* was used. The fat sample at the top of *figure 4* and the region defined by the yellow circle at the top of *figure 7* were also used. Taking the different scaling of the two images into account the mean pixel intensities of the regions of fat and water described above are given in the table below.

Table 3. A comparison of the mean pixel intensities of regions of fat and water in figures 4 and 7 (i.e. without and with fat suppression respectively).

Regions	Mean pixel intensity
Water – figure1 (fat unsuppressed)	19544
Fat – figure1 (fat unsuppressed)	9008
Water – figure 4 (Fat suppressed)	4648
Fat – figure 4 (Fat suppressed)	306

From this table the (fat/water) ratio for the unsuppressed image (*figure 4*) was found to be 0.46 and that for the suppressed image (*figure 7*) was found to be 0.07.

The unsuppressed to suppressed fat ratio was also calculated from the above values and was found to be ~30. The corresponding ratio for water in the different images was found to be ~ 4. Therefore fat suppression is ~ 7 times higher than water suppression between the two images. This shows that there has been considerable suppression of the fat using $T_{I\text{NULL}} = 140\text{ms}$ in the modified spin echo pulse sequence.

4 Conclusion

Two images were obtained using the standard pulse echo sequence with bandwidths of 25 kHz and 12.5 kHz. As the dark circles were observed to shift relative to water for the lower frequency image they were identified as corresponding to the fat samples. From this image the shifts for the four fat samples were calculated as -3.94, -3.63, -3.89 and -3.89 ppm. These values are all within 0.44ppm of the expected shift for this field strength.

By minimizing the contribution of the fat samples to the FIS, $T_{I_{NULL}}$ was found to be 140ms. This corresponds to a T_1 value of 201.6ms. This T_1 value is about 5 times shorter than TR and is about 5 times longer than TE.

Fat suppression was then attempted using the above value of $T_{I_{NULL}}$. This was quantified by calculating the fat/water signal of the unsuppressed and suppressed images. These were found to be 0.46 and 0.07 respectively. This indicates that considerable suppression of the fat signals had been achieved. However some suppression of the water has also taken place. Selection of a fat suppression technique should depend on the purpose of the fat suppression (contrast enhancement vs tissue characterization) and the amount of fat in the tissue being studied.

ACKNOWLEDGEMENTS

I would like to thank my supervisor Dr. Hugh Seton for his assistance and suggestions throughout this project. Without his advice, enthusiasm and patience, this work would never have been achieved.

REFERENCES

- [1] De Kerviler, E., et al. "Fat suppression techniques in MRI: an update." *Biomedicine & pharmacotherapy* 52.2 (1998): 69-75.
- [2] D. J. Blezek, W. T. Dixon and P. J. Dhawale, "Single image phase-based MRI fat suppression expectation maximization algorithm," *2005 IEEE Computer Society Conference on Computer Vision and Pattern Recognition (CVPR'05)*, 2005, pp. 540-546 vol. 2.
- [3] Bley, T. A., Wieben, O., François, C. J., Brittain, J. H. and Reeder, S. B. (2010), Fat and water magnetic resonance imaging. *J. Magn. Reson. Imaging*, 31: 4–18. doi:10.1002/jmri.21895.
- [4] Reeder, S. B., Yu, H., Johnson, J. W., Shimakawa, A., Brittain, J. H., Pelc, N. J., Beaulieu, C. F. and Gold, G. E. (2006), T_1 - and T_2 -weighted fast spin-echo imaging of the brachial plexus and cervical spine with IDEAL water–fat separation. *J. Magn. Reson. Imaging*, 24: 825–832. doi:10.1002/jmri.20721
- [5] Yu, H., Reeder, S. B., McKenzie, C. A., Brau, A. C. S., Shimakawa, A., Brittain, J. H. and Pelc, N. J. (2006), Single acquisition water-fat separation: Feasibility study for dynamic imaging. *Magn. Reson. Med.*, 55: 413–422. doi:10.1002/mrm.20771
- [6] Zhang, W., Goldhaber, D. M. and Kramer, D. M. (1996), Separation of water and fat MR images in a single scan at .35 T using „sandwich” echoes. *J. Magn. Reson. Imaging*, 6: 909–917. doi:10.1002/jmri.1880060612

- [7] Palosaari, Kari, et al. "Fat suppression gradient-echo magnetic resonance imaging of experimental articular cartilage lesions: Comparison between phase-contrast method at 0.23 T and chemical shift selective method at 1.5 T." *Journal of Magnetic Resonance Imaging* 18.2 (2003): 225-231.
- [8] Xiang, Q.-S. and An, L. (1997), Water-fat imaging with direct phase encoding. *J. Magn. Reson. Imaging*, 7: 1002–1015. doi:10.1002/jmri.1880070612
- [9] Ma, J., Vu, A. T., Son, J. B., Choi, H. and Hazle, J. D. (2006), Fat-suppressed three-dimensional dual echo dixon technique for contrast agent enhanced MRI. *J. Magn. Reson. Imaging*, 23: 36–41. doi:10.1002/jmri.20470
- [10] Miller, T. T., et al. "Fat-suppressed MRI of musculoskeletal infection: fast T2-weighted techniques versus gadolinium-enhanced T1-weighted images." *Skeletal radiology* 26.11 (1997): 654-658.
- [11] Reeder, Scott B., et al. "Quantitative assessment of liver fat with magnetic resonance imaging and spectroscopy." *Journal of magnetic resonance imaging* 34.4 (2011): 729-749.
- [12] Mirowitz, ScotiA, et al. "MR imaging of bone marrow lesions: relative conspicuousness on T1-weighted, fat-suppressed T2-weighted, and STIR images." *AJR. American journal of roentgenology* 162.1 (1994): 215-221.
- [13] Lavdas, Ioannis, et al. "Stripline resonator and preamplifier for preclinical magnetic resonance imaging at 4.7 T." *Magnetic Resonance Materials in Physics, Biology and Medicine* 24.6 (2011): 331-337.
- [14] Lin, Chen, Clark David Rogers, and Shadie Majidi. "Fat suppression techniques in breast magnetic resonance imaging: a critical comparison and state of the art." (2015).
- [15] Tien, Robert D. "Fat-suppression MR imaging in neuroradiology: techniques and clinical application." *AJR. American journal of roentgenology* 158.2 (1992): 369-379.

Comparative Study of Left Ventricular Low Wall Motion with Scar Tissue Using 4D Left Ventricular Cardiac Images

Chien-Yi Lee¹, Yashbir Singh¹, Michael Friebe², Wei-Chih Hu¹

¹Chung Yuan Christian University, Zhongli District, Taiwan 320

²Otto-von-Guericke-Universität, Magdeburg, Germany

ack20499@gmail.com; yashbir143@gmail.com; michel.friebe@ovgu.de; weichihhu@cycu.edu.tw

ABSTRACT

Myocardial contraction affects the cardiovascular pumping system, and helps in the early phase to detect abnormalities of wall motion noninvasively. In this research, we designed a program to characterize regional abnormalities because scar tissue is very difficult to identify in normal cardiac CT images. We created 10 frames of a 3D heart model that contains the long axis as reference for predicting the left ventricular wall motion. We tested our 4D cardiac model with scar tissue using non-invasive cardiac CT images. Here, four subjects (patients) were involved in this study. Subject 1 and 4 are matching the low motion of surgical area with scar tissue area. Subject 2 found fibrous tissue regions (about 40%), compared with the 2SD (Standard Deviation) region. The fibrotic area is completely overlapped with a low-motion region which indicates the fibrotic area has a significant correlation with the low wall motion region. This research evaluates low wall motion of the left ventricle and detection of fibrosis regions.

Keywords: Left ventricular remodeling; myocardial wall motion; Cardiac imaging; Fibrotic tissue; Noninvasive cardiac evaluation;

5 Introduction

Cardiac disease has become a very challenging clinical problem like regional myocardial injury. It is one of the goals of cardiac imaging methods to measure the regional function of the left ventricle (LV). There are many existing techniques to precise and reliable quantitative regional LV function measurements. Most of the standard methods depend on 2D image sequence data [1, 2, 3, 4, 5, 6]. Most of the techniques have been used end-diastolic (ED) and end systolic (ES) image frames. While the LV expansion and LV thickening from region to region is indicative of ischemia [2, 4, 6]. Song and Leahy have performed the dense-field optical flow approach to include fluid flow models using 3D datasets [7]. The Goldgof research group followed a shape matching idea which is similar to ours; though they primarily use Gaussian curvature employing conformal stretching models [8]. Pentland and Terzopoulos have been studying non-rigid motion models, using finite element analysis, which might be useful for cardiac analysis. The Ayache group unified these two approaches to segment and track the object simultaneously [9]. A recently proposed technique is the use of phase contrast MR images to decipher local velocity [10]. However, MR images take a long in acquisition and resolution is less than CT images. This can be integrated to estimate trajectories of individual points over time [11, 12]. Our new

developments could potentially help in curvature estimation, point-wise non-rigid motion tracking, initial quantitative measures of LV motion, thickening, and 3D visualization techniques. The experimental results from real image sequences of multi-phase and multi-slice cardio CT image will be presented, and future research directions will be discussed.

2 Methods

This is a Comparative study of low wall motion with scar tissue using 4D left ventricular cardiac images. The methodology has been grouped into various categories:

Data Extraction

We used Microsoft Windows 7, the 64-bit platform with Intel Celeron CPU G550, memory DDR3 4GB, Visual C ++ 6.0 MFC4.2 for software development and OpenGL library as a tool for the 3D model [13]. Images were obtained from the Philips computerized tomography (CT) instrument provided by the National Institute of Hospital of Yang-Ming University. This study and the informed consent procedure were approved by the Institutional Review Board of National Yang-Ming University Hospital. Each subject has 10 sets of timing frames, including a complete heartbeat cycle. 1 set of 3D cardiac image has 400 slice of cardiac CT images. The scanned image size is 512×512 (pixels). 1 voxel is 0.165 mm^3 ($0.429 \times 0.429 \times 0.9$) where ($x \times y \times z$). We used this images to extract edges of endocardium and estimated the endocardium area of LV. In this way, we find the change of edges of wall motion.

The program flow is as follows:

- Read the image into the program, confirm the format for the DICOM (Digital Imaging and Communications in Medicine), the image is 512x512gray form stored in the program.
- 3D reorganization and image information is obtained to construct the stereoscopic model of the thoracic area. Set the left ventricular central axis and resample the image [13].
- Perform a manual split using our program at the first slice only then use the regional growth law circle, draw the contour of the left ventricular endocardium.
- The endocardial shape of the LV endocardium is magnified at a variable magnification, and the boundary of the second regional growth is made.
- Repeated manual segmentation is performed to obtain epicardial information. 3D model LV endocardium and epicardium is established by a triangular mesh [14, 15].

Left Ventricular Edge Search

We use manually cutting of LV images from base to apical from the entire data set, selected one image from the dataset and one seeded point to start this process. We obtained the geometrical center that connects each slice on long axis, applied regression calculation to find the line as a reference axis for LV [16, 17].

Manually Divide the left Ventricle

In this section, we performed re-sampling of the images to find the short axis, separated LV from aorta (Fig 1).

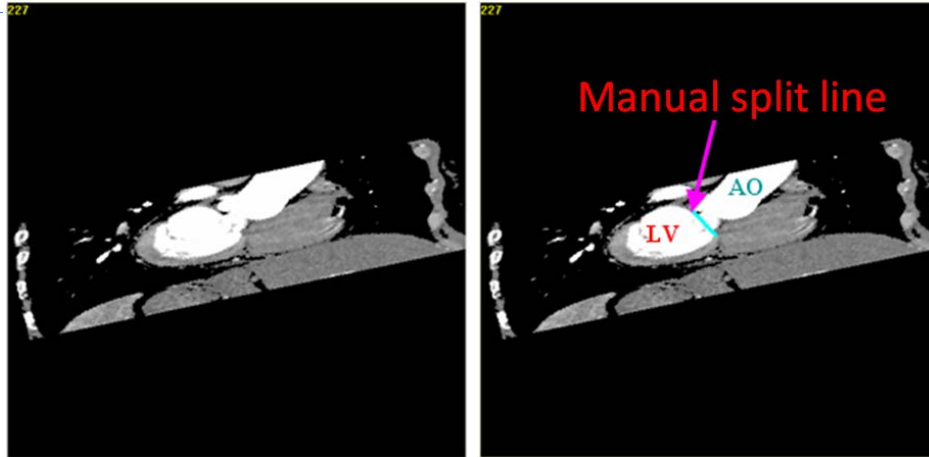


Figure 1. Manually separated line between left ventricle and the aorta.

Regional Growth Circle Selected Endocardium

In this study, the left ventricular endocardial circle is used for the regional growth of the image which is close to the edge of the image. The regional growth of the operation is needed to set up the initial seed point. The initial point of the first slice will be considered as the reference point of the second slice, the second reference point will be set as the seeded region for other layers simultaneously (Fig 2) [16, 17]. It is necessary to confirm that the seeded spots of each layer are in the endometrial region, if not, we need to manually correct the seed points.

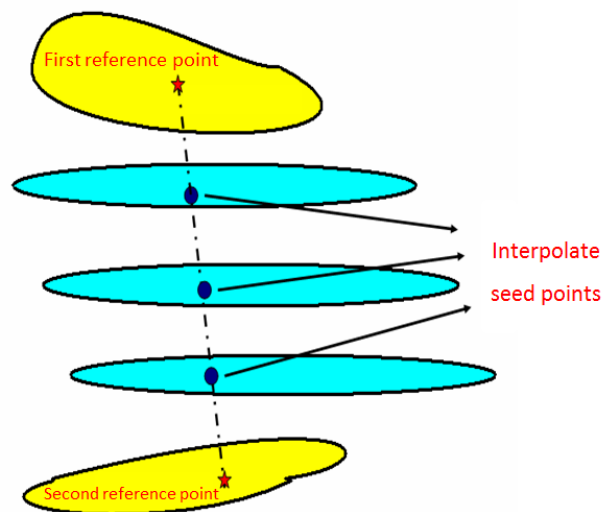


Figure 2. Seeded Point Star from the First Layer and The Last Layer.

Simulation Study

The simulation model is proposed by Yang Bochuan and Ma Minghui. We obtained LV endocardium and the outer membrane Lattice model at different time of the long axis, calculated the diastolic and systolic period of the radius between the rates of change. After that we obtained the number of myocardial changes at each time. These steps are to obtain the simulated left ventricular at each time. This stereoscopic model is to simulate the changes of the LV in the cardiac cycle and the different values of myocardial changes in each block [18].

Triangular Mesh

We use triangular mesh for LV endometrial and adventitial information 3D. The number of samples for the study of 31 layers of each layer of 30 points a total of 930 points, which defines 1 to 10 layers for the base, 11 to 20 layers is the top layer, the 21-30 layers is the middle layer, and the 31st floor is the reference layer. The sampling method divides the total number of the left ventricles by 31 layers, and stores the coordinate points (X, Y, Z). The simulation is to use these 930 points to do the simulation movement. We calculate the momentum information of the heart when the low amount of movement occurs [15, 19].

Simulated Model End of Diastolic Phase

LV contracts at the centre axis. The endometrial and adventitial information goes the left ventricular central axis to establish a triangular mesh model (Fig 3), which shows the gap between outer membrane model and the endometrial model. 10 frame of the triangular mesh is done. In the endometrial triangular mesh model found with the degree of myocardial changes in different levels of red, yellow, green, light blue and dark blue are five colors (Fig.4), and will record the picture in the dark blue block coordinates.

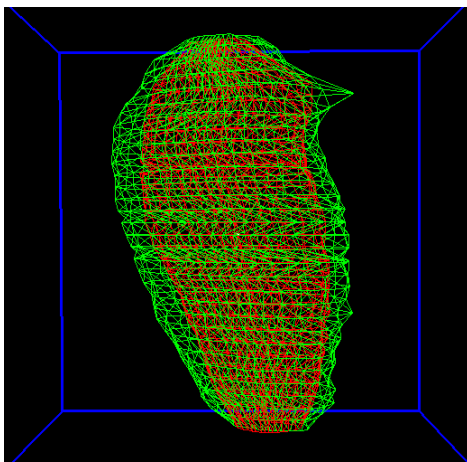


Figure.3 Left Ventricular Triangular Mesh Simulated Model that represents green color for outer membrane model, red for the endometrial model.

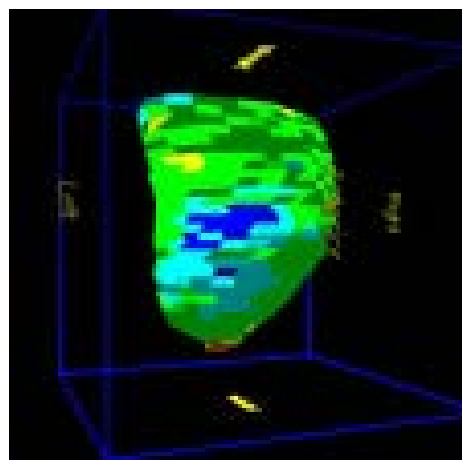


Figure.4 Simulation model of left ventricular motion analysis.

Fibrosis Area Assessment Interface

This study explores the relationship between regional and motion. Hiroaki and other scholars performed the method using patient's delayed-enhancement images that determined the area of fibrotic tissue. This interface exhibit the calculation within the region of the HU (Hounsfield unit) average or press the single click in the block on the right mouse button, point to the center of the circle to 10 points for the radius of the circle. It automatically calculates the circle within the HU average and pink color display in the circular area (Fig.5). We get the region of interest HU value which shows region of fibrosis. This experiment performed to find the fibrosis area [20, 21].

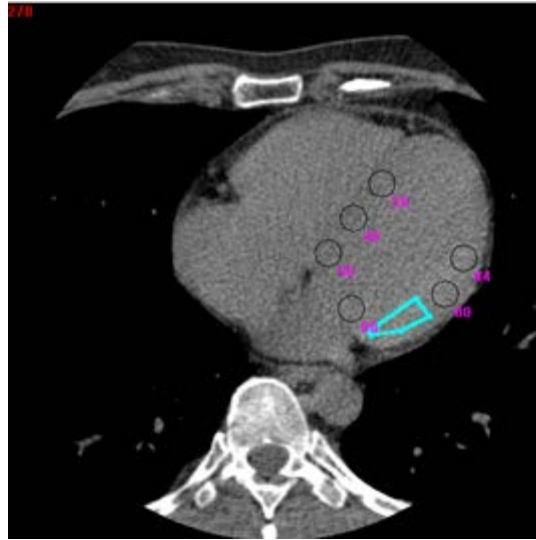


Figure.5 Fibrous area assessment interface (Pink circle area is the HU value of the manual selection area).

3 Results

Motion Model Analysis Interface

We determined 10 lattice grid models in the DICOM 0 timing to reconstruct 3D heart volume and executed the program. We get a 4D model of LV motion. This display interface allows the user to observe the three-dimensional model of the inner portion of the left ventricle (Fig 6). The red color model represents a 3D model of the inner membrane, whereas the green color model represents the three-dimensional model of the outer membrane. This simulation system exhibits the LV outer membrane state of motion (Fig.7) which provides better understanding of the movement of the myocardium in the LV. This method is used dynamically to increase the number of left ventricle models in a linear interpolation method.

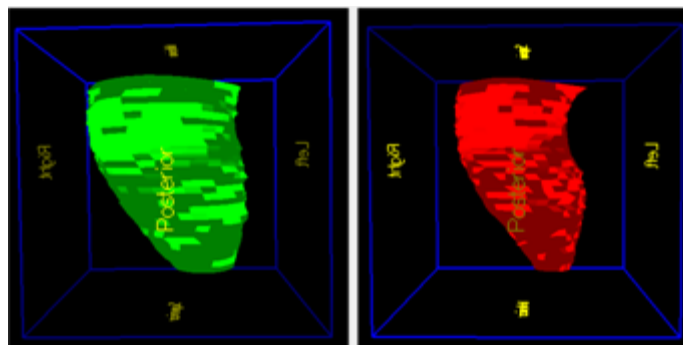


Figure.6 Analog interfaces (The red color model represents inner membrane of 3D, green color model represents outer membrane of 3D).

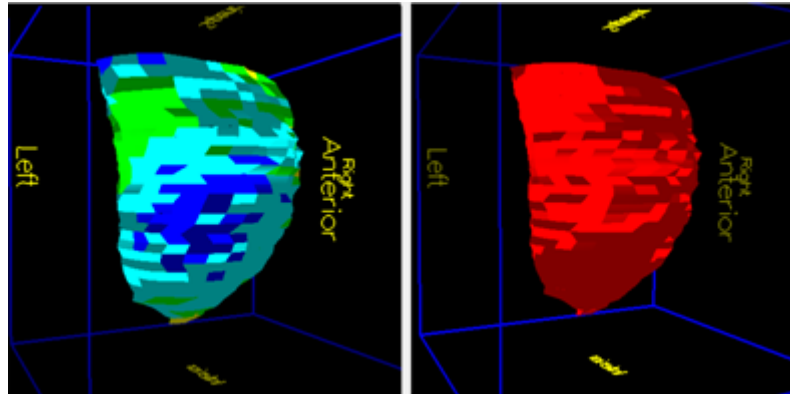


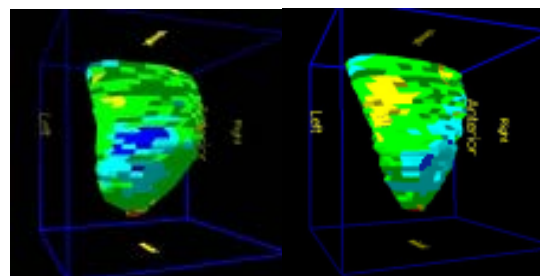
Figure.7 Dynamic interface diagram.

left Ventricular Low Motion Region Assessment

Different color areas represent the difference between the mean left ventricular displacements. The blue is the relative displacement of 2 mm or less, the light blue is the displacement 2 ~ 3 mm, green is the displacement of 3 ~ 4 mm, yellow is the displacement of 4 ~ 5mm, red is the displacement of more than 5mm, and low-motion area is defined as the average amount of difference between the value of less than 2mm area. This study re-sampled after the left ventricular model 1 to 10 layers defined as the base layer, 11 to 20 layers is defined as the middle layer, 21 to 30 layers defined as the top layer. The method takes 30 points of sampling points counterclockwise (Fig. 8) (Fig. 9) (Table. 1).

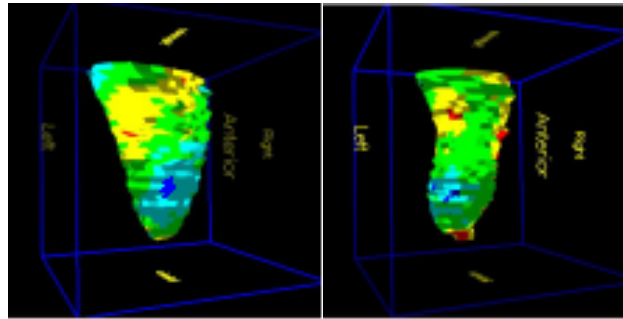


Figure.8 Re-sampling the sampling point.



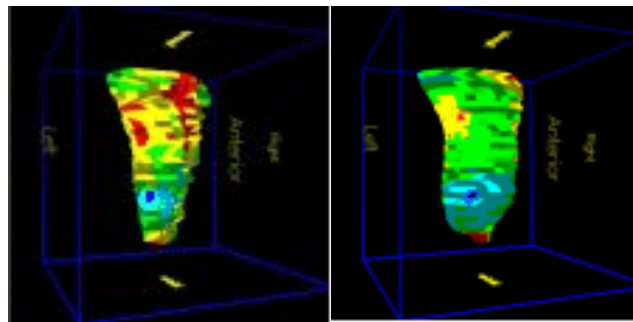
Timing series 0

Timing series 1.



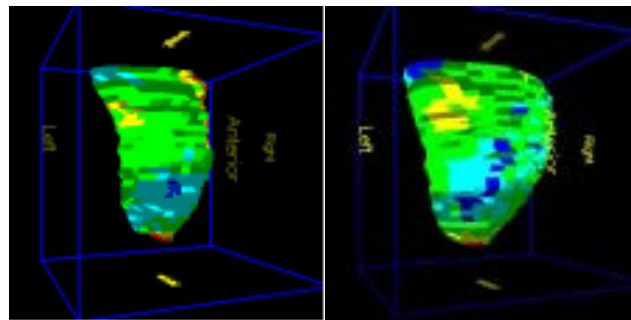
Timing series 2

Timing series 3.



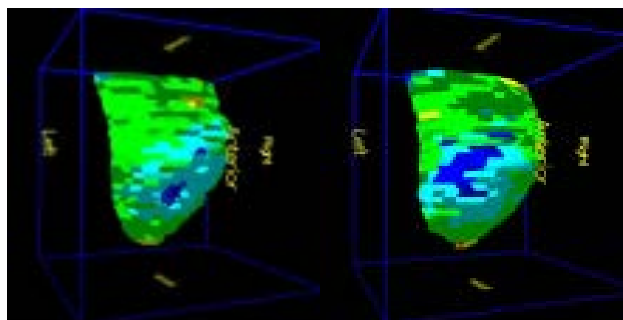
Timing series 4

Timing series 5.



Timing series 6

Timing series 7.



Timing series 8

Timing series 9.

Figure.9 Myocardial changes in the model of subject 1 at every time series.

Table.1 Analysis result

Patients	Generation layer	Segment group location	Point shift	Position evaluation
Subject1	8	Segment 23, Degree 276	1.712mm	Middle layer Posterior side
		Segments 24, Degree 288	1.784mm	
		Segments 23, Degree 276	1.672mm	
	9	Segments 24, 288 degree	1.559mm	
		Segments 25, 300 degree	1.588mm	
		Segments 26, 312 degree	1.576mm	
		Segments 23, 276 degree	1.695mm	
	10	Segments 24, 288 degree	1.701mm	
		Segments 25, 300 degree	1.543mm	
	11	Segments 24, 288 degree	1.728mm	

We observed the low-motion region in the LV (Table .2) and defined 1 to 15 points for the front side (inferior), 16 to 30 points for the back (inferior), each interval is 12 degrees sampling points. In addition, the movement model analysis interface calculated with low sequence (Table.3).

Table. 2 Location of scar tissue in the patients after surgery.

Number of patients	Number of layers	area
Subject1	Middle layer	Posterior side
Subject2	Middle layer	Anterior side, posterior side
Subject3	Lower Layer	Posterior side
Subject4	Lower Layer	Anterior side

Table.3 Detection of the fibrotic tissue location.

No. of Patients	HU (Avg)	(Std Devi)	Greater than 2SD layers	Area
Subject1	60.2	8.4	266~274(middle layer)	Posterior side
Subject2	58.7	7.9	271~283(Middle layer)	Anterior side
Subject3	71.3	12.1	No	no
Subject4	64.5	9.0	302~309(base layer)	Anterior side

Determination of left Ventricular Fibrosis Area

We performed patient's surgery of LV site. Using meglumine diatrizoate, we developed enhancement image criteria using Zeinab et al, found the information of the single image with a fibrotic area, scanned the 10-slice and 20-slice myocardial wall area to ensure that the post-operative area in the left ventricle pattern which is defined by the spinal cord for the posterior Side. It contains the lower wall of the hypopharynx, inferior wall, back wall and front of the spinal cord that contains septal, anterior wall and other blocks. We scan whole heart during the systolic phase and find the area which has low changing radius to match the scar area as low wall motion area. The changing radius is 7.76% which is less than the average changing radius that exhibits low wall motion of LV. The assessment of impaired myocardial function is compared to the central axis angle. Low-motion region is only related to the change in the radius. Therefore, this study shows that the maximum low-motion area, affect the central axis angle changes. The low-volume region is the fibrotic area; results are found (Table. 4).

Table 4. Descriptive result of Subject 1.

Individual	The layer of surgical position	Surgical area	The slice of left ventricle	HU value is greater than the average 2SD area(HU value>77)	Resample the model layer	Point group location	Point group displacement
Subject1	Middle layer	Posterior	266 slice	No	Eleventh	The 23rd point(Degree 276)	1.712mm
			267 slice	No			
			268 slice	Degree 264(HU value85) Degree 276(HU value77) Degree 264(HU value86) Degree 276(HU value92)			
			269 slice	Degree 336(HU value79) Degree 348(HU value77) Degree 264(HU value89) Degree 276(HU value92)		The 24th point(Degree 288)	1.784mm
			270 slice	Degree 288 (HU value83) Degree 312(HU value79) Degree 336(HU value79) Degree 252(HU value80) Degree 264(HU value90)			
			271 slice	Degree 276(HU value83) Degree 348 (HU value78) Degree 324(HU value85) Degree 252(HU value79) Degree 264(HU value84)		The 23rd point(Degree 276)	1.672mm
			272 slice	Degree 336(HU value79) Degree 348(HU value82) Degree 264(HU value84)		The 24rd point(Degree 288)	1.559mm
			273 slice	Degree 276(HU value79) Degree 348(HU value81) Degree 264(HU value80)		The 25rd point(Degree 300)	1.588mm
			274 slice	Degree 276(HU value77) Degree 348(HU value77)		The 26rd point(Degree 312)	1.576mm
			275 slice	No		Ninth	The 23rd point(Degree
276 slice	No						

277 slice	No		276) The 24rd point(Degree 288)	1.701mm
278 slice	No		The 25rd	
279 slice	No		point(Degree 300)	1.543mm
280 slice	No			
281 slice	No			
282 slice	No		The 24th	
283 slice	No	Eighth	point(Degree 288)	1.728mm
284 slice	No			
285 slice	No			

We have four Subjects (Patients), Subject 1 and 4 are matching the low motion of surgical area with scar tissue area. Patient 2 has five districts surgical area, the presence of fibrous tissue is only two regions (about 40%), compared with the 2SD (Standard Deviation) region. The region is higher than the average of 1.6 to 1.8 times the SD value produced. Compared with larger than 2SD region, a slow-motion region found, the fibrotic area completely overlapped with a low-motion region which indicates the fibrotic area. It has a significant correlation with the low-motion region. This study is also found that the fibrosis area is significantly lower than low exercise area. Injured area involved in the movement of adjacent muscles which led to low mobility area than the fibrosis area to the wide. Subject 3 is no fibrotic tissue in this region, as long as the myocardial injury to a certain extent will lead to low motion incidence of the region, but the system can still find the low motion region and position. Only the low-motion area is the medium-risk group in the non-scar area. This study is compared with the fibrotic area method which is proposed by the previous research, our study is to detect the low motion area. It is possible to predict the location of the fibrosis region by irradiating the delayed-enhancement image. The tool can further identify the area of low motion activity without fibrosis, which is performed by the physician for early monitoring, and tracking can provide effective help.

4 Conclusion

This research evaluated low wall motion of the left ventricle of the four patients after surgery, myocardial changes analysis and fibrosis of the region confirms the feasibility of the myocardial movement. This method is sensitive to detect the myocardium dysfunction. We can apply this method to find different types of ventricle disease of the cardiomyopathy. This study is included the assessment of myocardial infarction, Cardiac remodeling and assessing the role of fibrotic tissue in the heart. Further research will involve the integration of the heart motion, validating geometrical landmarks and integration of the motion matching.

REFERENCES

- [1] J. Areeda, E. Garcia, K. Vantrain, D. Brown, A. Waxman and D. Berman. A comprehensive method for automatic analysis of rest/exercise ventricular function from radionuclide angiography. *Digital Imaging: Clinical Advances in Nuclear Medicine*, 1982.
- [2] E. L. Bolson et al. Left ventricular segmental wall motion - A new method using local direction information. *The computer in Cardiology*, 1980.
- [3] I. Clayton et al. The characteristic sequence for the onset of contraction in the normal left ventricle. *Circulation*, 1979, 59:671.

- [4] H. Gelberg et al. Quantitative left ventricular wall motion analysis: A comparison of area, chord, and radical methods. *Circulation*, 1979, 59:991-1000.
- [5] C. Slager et al. Quantitative assessment of regional left ventricular motion using endocardial landmarks. *JA CC*, 1986.
- [6] D. Zisserman et al. Cardiac catheterization and angiographic analysis computer applications. *Progress in Cardiovascular Diseases*, 1983.
- [7] S. Song and R. Leahy. Computation of **3D** velocity fields from **3D** cine CT images. *IEEE Transactions on Medical Imaging*, 1991.
- [8] C. Kambhamettu and D. Goldgof. Point correspondence recovery in non-rigid motion. *IEEE Computer Vision and Pattern Recognition*, 1992, 222- 227.
- [9] A. Pentland and B. Horowitz. Recovery of nonrigid motion and structure. *IEEE Transactions on Pattern Analysis and Machine Intelligence*, 1991.
- [10] D. Terzopoulos and D. Metaxas. Dynamic 3D models with local and global deformations: deformable superquadrics. *IEEE Transactions on Pattern Analysis and Machine Intelligence*, 1991
- [11] N. J. Pelc, A. Shimakawa and G. H. Glover. Phase contrast cine MRI. *Proceedings of the 8th Annual SMRM*, 1989.
- [12] J. van Welden, G. Holmvang, H. Kantor and T. J. Brady. Measurement of myocardial strain with phase sensitive MR. *Proceedings of the 9th Annual SMRM*, 1990.
- [13] W. J. Richard S., "OpenGL Super Bible," 1996.
- [14] Monga and N. Ayache. From voxel to curvature. *IEEE Computer Vision and Pattern Recognition*, 1991, 644-649.
- [15] P. T. Sander and S. W. Zucker. Inferring surface trace and differential structure from **3D** images. *IEEE Transactions on Pattern Analysis and Machine Intelligence*, 1990, 12(9):833-854.
- [16] J. Park, D. Metaxas, A. A. Young, and L. Axel, "Deformable models with parameter functions for cardiac motion analysis from tagged MRI data," *IEEE Transactions on Medical Imaging*, 1996.
- [17] J. Huang, D. Abendschein, V. G. Davila-Roman, and A. A. Amini, "Spatio-temporal tracking of myocardial deformations with a 4-D B-spline model from tagged MRI," *IEEE Transactions on Medical Imaging*, 1999.
- [18] M. F. Smith, "The effect of contraction and twist on myocardial PET and SPECT image resolution: a mathematical phantom study," *IEEE transactions on nuclear science*, 2000.
- [19] L. H. Staib and J. S. Duncan. Deformable Fourier models for surface finding in **3D** images. *SPIE Vol. 1808: Visualization a Biomedical Computing*, 1992.
- [20] Fearmonti, R., Bond, J., Erdmann, D., & Levinson, H. A review of scar scales and scar measuring devices. Eplasty, 2010.
- [21] Razi, T., Niknami, M., & Ghazani, F. A. Relationship between Hounsfield unit in CT scan and grayscale in CBCT. *Journal of dental research, dental clinics, dental prospects*, 2014.

External Group Labeling of Objects in 2D Medical Images Using Spring-Mass Model

¹Muhammad Masud Tarek, ²Bilkis Jamal Ferdosi

¹Associate Professor, Department of CSE,
State University of Bangladesh, Dhaka, Bangladesh

²Associate Professor, Department of CSE,
University of Asia Pacific, Dhaka, Bangladesh
tarek@sub.edu.bd; bjferdosi@uap-bd.edu;

ABSTRACT

The parallel processing of verbal elements like textual labels, annotations etc. with non-verbal i.e. visual elements, provides maximum integration of human mind. Textual labels and annotations aid in understanding medical data visualization. But it is a very challenging task to generate hand-made like illustration labels in an automated system. The paper presents a noble approach for dynamic external labeling of segmented 2D computer tomography (CT) slices. Various efficient algorithms are approached to solve labeling problems in modular form. The system emphasizes on the readability and clarity of labels while generating dynamic group labels in real time for 2D slices using external labeling layout.

Keywords: External labels, medical data visualization.

1 Introduction

Images are considered as a very powerful medium for communicating ideas. However to make an image more meaningful and informative, textual descriptions such as labels, legends, captions etc. have become essential parts of images, especially in educational and scientific documents. Labels are largely classified as internal and external labels. Internal labels are placed within the objects of a picture. On the other hand, external labels are placed into the empty spaces, outside of the objects. Both internal and external labels are used to describe or distinguish different graphical elements. In case of external labels, lines are drawn between labels and their corresponding referenced objects. As aesthetic is a very important factor, illustrators have to be very careful to maintain the visual balance while labeling a handmade illustration. Automated and interactive labeling systems are still a challenge. Poor placement of labels may have a negative impact on understanding a visual system. Whether it is an interactive or automated system, the main goal of labeling an illustration is to employ any of the layout conventions that are used by human illustrators, so that labels can be read comfortably and visual balance of the image is preserved.

For quantitative measurement, segmentation of computer tomography (CT) is needed by many image analysis procedures. Research are going on to produce CT segmented images [12, 13]. Different segmentation masks are used to distinguish background and different structures. In real life application,

DOI: 10.14738/jbemi.52.4445

Publication Date: 29th April 2018

URL: <http://dx.doi.org/10.14738/jbemi.52.4445>

doctors sometimes need a verbal description of the segmented structures. Also, medical students need textual contents along with the CT images for better understanding. Manual labeling would be a naïve way for this type of application as hundreds of labels might need to be generated on the fly during analyzing CT images slice by slice. So here, a dynamic label placement system is developed which can generate external textual labels for segmented CT images. The system finds good placements of labels while viewing 2D slices with the consideration of different labeling aspects.

In section 2, some related works are reviewed. Section 3 states the system architecture while section 4 describes the developed dynamic labeling system. Section 5 provides some results with the discussion. Finally, the paper concludes with some hints of future extension.

2 Related Works

Dynamic textual labeling for CT images is still largely unexplored. However, there are some interactive systems for 3D models that address some of the labeling problems. For example, Zoom Illustrator [15] uses dedicated part on the screen for text so that they do not overlap any image object. Also, Fish View Technique [8] is used to show more textual information without overlapping other labels. Talking Shadows [4] and Illustrative Shadows [16] use object shadows for placing text information of the associated objects. But they hardly address any labeling layout problem.

A Virtual Reality application, View Management [3] dynamically places labels for objects. It considers most of the labeling problems such as internal or external labeling layout, empty space management, minimization of label overlapping etc. However, as it uses bounding box technique to determine the area of an object, thin long diagonal objects may wrongly occlude other small objects. Map labeling is a well-studied field and many works are done for dynamic internal map labeling layout. However, it is found that global optimization (i.e. no overlapping of labels) is computationally N-P hard [6]. So, change of one label position effects the entire map labeling layout.

Few good algorithms are developed for 3D dynamic labeling. They consider major labeling layout problems such as label layouts (flash or radial, internal or external), placement of external labels into empty space, minimization of line crossings, elimination of label overlapping etc. Floating Labels [10] uses some potential force fields to eliminate overlapping of labels. It also addresses frame coherency to minimize visual discontinuity. In [9], calmer parts of the animated 3D objects are determined where anchor points or internal labels can be put to achieve lesser flickers among frames. Ali et al. [1] employed different layout methods for external labeling of 3D illustrations. The system is greatly suitable for compact and convex 3D models with having enough empty spaces surrounding the object. These techniques can be adopted for 2D layered CT images with considerations. However, achieving all the aesthetic criteria of a labeling layout at the same time is very difficult as some criteria may conflict each other. Also most approaches trade-off between labeling quality and computational costs.

Oeltze-Jafra and Preim surveyed several techniques of labeling in medical visualization [20]. They proposed a categorization of different labeling techniques and recommended guidelines for choosing a proper technique for a specific type of application area. They indicated that it is a hard task to achieve all requirements of labeling. They also reported that among several techniques labeling slice views is a relatively less explored area.

In [21] Kang et al. proposed a force-directed labeling method for 3D street visualization that increases the visibility of street addresses in the map. However they addressed the problem of internal labeling whereas our method address the problem of internal labeling.

3 System Architecture

After reviewing related works and analyzing medical illustrations [17, 19] it is found that a good labeling system should consider the following aspects:

Readability: Labels and lines should have good background contrast. Font size, text shadow, background and foreground color can be adjusted by the users as needed.

Aestheticism: Placement of the labels should be such that there should not be any overlapped label. Also, line crossings should be eliminated or reduced. Anchor points should be at salient positions of the structures.

Efficiency: Good, efficient algorithm should be used so that the system can be implemented for real-time application.

Grouping: Same structure may be seen in different places. Some criteria should be utilized to group them together and thus minimizes the number of labels.

Slice Coherency: Sizes, locations of structures may vary within different slices. So it is likely to vary the position of labels also, which may generate the blinking effect. So measures should be taken to minimize this blinking effect.

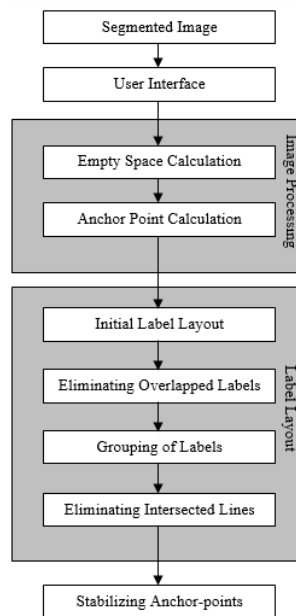


Figure 1: System Architecture

The system architecture (Fig. 1) is designed to achieve the above mentioned global requirements. The input segmented image itself contains the identification text (labels) and other color-coded information for each object, while users can define various label properties such as text size, color, text-background

color, and transparency etc. in the *User Interface (UI)* module. In the *Image Processing* modules, available empty spaces (i.e. background) are calculated where labels can be put. Acceptable anchor points for each object are also calculated here. A textual label is connected to an anchor point by a line to indicate the corresponding object. In the label layout modules, initial placement of each label is determined. Here, there are several other modules for eliminating label overlapping, grouping and eliminating intersection of connected line segments and thus final placements of all the labels of a slice are determined. The last module stabilizes anchor points to reduce visual discontinuity between two adjacent slices.

4 The Dynamic Labeling System

A modular approach is used to implement the dynamic labeling system. For the better contrast between image and textual labels, each label is enclosed within a rectangular box. The size of the box depends on the text length and font size of the label. Users are able to change rectangle background color on the fly (Fig. 2). For the aesthetic reason, these rectangle boxes are transparent, so that some parts of the graphical structures are visualized and thus minimizing visual clutter. Alpha Blending [14] is used for the transparency effect using the equation 1:

$$\begin{aligned} \text{NewPixelValue} &= BG * (1 - \alpha) + FG * (\alpha) \\ \text{where } BG &= \text{background pixel value} \\ FG &= \text{foreground pixel value} \\ \alpha &= 0 \text{ to } 1 \end{aligned} \tag{1}$$

For each slice, the generalized algorithm is:

1. Calculate background spaces which are available for putting labels
2. Identify each object uniquely
3. Calculate anchor point for each object
4. Determine initial label placement
5. Eliminate label overlapping by either
 - a. moving overlapped labels up or down repetitively to a minimum distance, or
 - b. using potential repulsive forces among labels and attractive forces between an anchor point and corresponding textual label of an object
6. Group same objects under a single textual label if those objects are within a threshold distance
7. Draw connection line from anchor points to their associated label
8. Eliminate connected line intersections
9. Stabilize anchor points of next slice if they are within a threshold value of current slice.

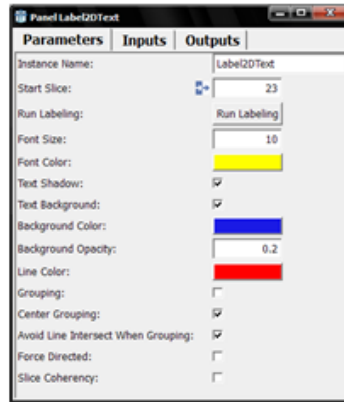


Figure 2: User Interface

4.1 Uniquely Identifying an Object

In a segmented CT slice, objects are color-coded uniquely but the same object (i.e. same color code) may appear in different places within a slice. For a successful labeling, each part has to be uniquely identified. Connected component labeling algorithm [5] may be used for that purpose. But if objects have many edges, a sheer amount of data in the equivalent table have to be managed which is extremely difficult. So here the system scans 8-neighbors of a pixel recursively to determine the area of an object. The algorithm is fast enough for a real-time system as a flag variable is used to avoid additional scanning of a pixel.

4.2 Anchor Point Calculation

The point of the object up to which the line from a textual label is drawn is known as an anchor point. As placement of a label depends upon anchor point position, a good calculation is much needed. For a fast output, any point of an object could be used as an anchor point. But it would not be an aesthetic choice. In [15], some criteria are discussed that should be taken into account during anchor point computation. For example, the point should be valid i.e. part of the corresponding structure. To avoid overlapping and visual clutter, anchor points should not cluster together and of course, calculations should be fast enough for an interactive system. Most importantly, it should be a salient point, i.e. at the visually most dominant part of the object. Skeletonization [11] is a good approach to find a salient point but computationally very expensive $O(n^2)$. To meet most of the criteria, the system uses the most inner point of an object as the anchor point using distance transform mapping [18] with computational cost $O(n)$. To avoid real number calculation, Euclidean or city-block distance matrices are avoided. Instead, Pseudo-Euclidean method [2] is implemented which uses integer approximation. It would not give actual distance (which is not required for this system) but the most inner point of an object can be determined efficiently.

4.3 Label Placement

For simplicity, the system uses flash left-right labeling layout. So, a label will be placed either left or right side of an object. Initially, after sorting all the anchor points of a slice, the system would try to place labels from top to bottom one by one. If the anchor point is at the left side of the slice, the system would try to find enough empty space at the left side of the object for the label. If failed, it would place

on the other side. Initially, a label is placed at the same y-coordinate of the associated anchor point. If any two labels are overlapped, they would be moved up or down at a minimum distance. The value of the minimum distance can be chosen by the user. Other already placed labels would be rechecked repeatedly to ensure no overlapping is happened (Fig. 3a).

The system can also use force-directed method for the placement of labels. Fruchterman and Reingold introduced a spring-embedding approach for graph drawing which considers two forces [7]. The attractive force attracts the connected vertices each other while the repulsive force causes all other vertices to repel each other. The same approach can be used for the external labels. Here a label is attracted by associated anchor point, whereas, labels have repulsive forces to each other. To avoid the collapse of a label to its object, all the pixels of that object except anchor point have repulsive forces on the label. Also, labels get repulsion from image boundary walls so that they will always be within the image area.

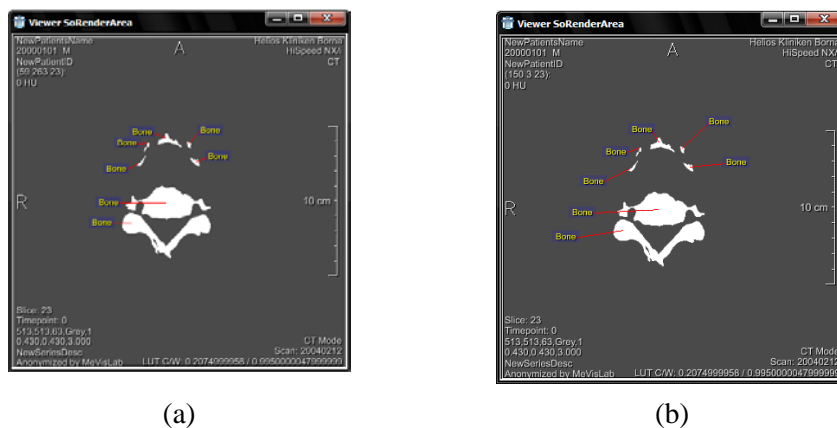


Figure 3: (a) Without force-directed method labels are put closer, (b) Force directed approach puts labels more uniformly

To employ the graph drawing method, labels are considered as zero length points. The attractive force between an anchor point and associated label can be given by,

$F_a(x) = x^2/k$ where x is the distance between the anchor point and the label and k is the tolerable distance between them. Typically the value of k is 30 to 50. Similarly, repulsion forces among labels can be calculated by,

$F_r(x) = -k^2/x$ where x is the distance between two labels and k is the ideal distance between them.

All forces are summed up to calculate the displacement for a label (Fig. 3b). However, a temperature t is used to control the displacement. At first, the temperature is given high (1.0) and a cooling function is used to cool it in each iteration. The typical cooling rate is 0.95 to 0.90. During iteration minimum of temperature and normalized force value is used for a small displacement of the label. Typically, after 20 to 30 iteration a satisfactory label placement can be achieved (Algorithm 1).

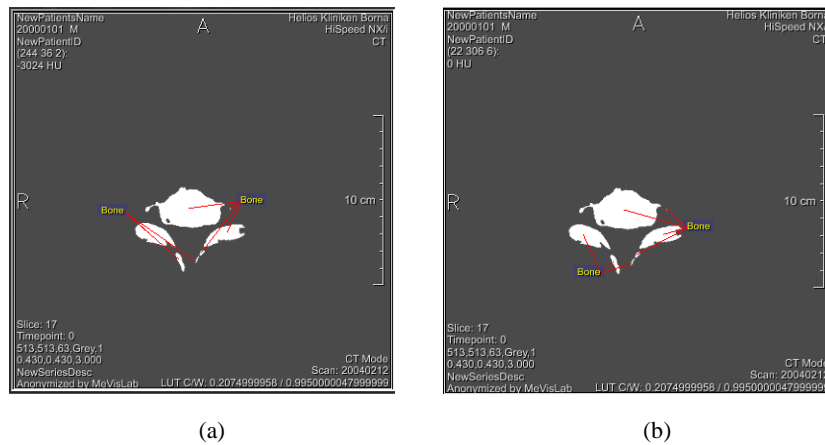


Figure 4: Grouping (a) without and (b) with considering the centroid of anchor points.

4.4 Grouping

In a CT slice, same object (or structure) may appear more than once. Sometimes it is desirable to group those objects under one label. This would make the output image more readable. However, it may not always produce a good result. Many objects under one label may cause visual clutter. So, for grouping of labels, we consider some criteria such as the number of maximal objects that can be grouped together, maximum distances among group objects etc. The real challenge is the good placement of label for a group of objects. One simple approach is to take the initial label position of the most upper object of the group. But it would not give a salient position. So the system uses more complex approach. Here, the centroid of the candidate anchor points is calculated. The initial label of the nearest anchor point of the centroid is served as the label of all group members. All other labels are deleted and connection lines are redrawn from the selected label to anchor points (Fig. 4).

Algorithm 1: Force-directed method

L = list of labels

A = anchor points

W = boundary points of the slice

O = list of objects' border points

for iteration:=1 to max_iteration // typically, max_iteration=20 to 30

 for each L[i]

 TDisp[i]:=0

 // a label attracts its referenced anchor point

 Disp:=L[i]-A[i]

 TDisp[i]:= TDisp[i]- sign(Disp)* AForce(abs(Disp))

 for each L[j]

 if (i!=j)

 // a label repulses other labels

 Disp:=L[i]-L[j]

 TDisp[i]:= TDisp[i]+ sign(Disp)* RForce(abs(Disp))

```
// a label repulses non-referenced anchor points
Disp:=L[i]-A[j]
TDisp[i]:= TDisp[i]+ sign(Disp)* RForce(abs(Disp))
end if
end for
// a label repulses slice-border points
for each W[j]
Disp:=L[i]-W[j]
TDisp[i]:= TDisp[i]+ sign(Disp)* RForce(abs(Disp))
end for
// a label repulses its object's border points
for each O[i]
Disp:=L[i]-O[i]
TDisp[i]:= TDisp[i]+ sign(Disp)* RForce(abs(Disp))
end for
// calculate new label position with initially, Temperature=1
EffectiveDisp:= sign(TDisp[i]) * min(norm(TDisp), Temp)
L[i].pos:=L[i].pos + EffectiveDisp
Temp=cool(Temp)
end for
end for

function AForce(x){return k2/x;} // k=ideal distance
function RForce(x){return x2/k;} // k=tolerable distance
function cool(temperature) {return temperature * coolingRate;}
//initially temperature=1.0, typical coolingRate=0.95
```

4.5 Eliminating Line Intersections

Using elementary geometry knowledge, each pair of line segments are checked for any intersections. For non-group labels, if any intersection is found, label positions are swapped, thus eliminating line intersections. After swapping, corresponding segment is again re-checked with other lines. As a number of labels within a slice are not much (usually less than 30), so the above-mentioned method can be used in real time system without much difficulty. For grouped labels, if any intersection occurs, it would be more complex to solve. In that case, the object which is responsible for line intersection is left out from the group.

4.6 Slice Coherency

The system generates labels dynamically according to objects' location, computed anchor points and available empty spaces. When users go through slices interactively, it is more desirable to have a minimal change of label locations. The abrupt change of labels may generate flicker and users' attention may be destructed. If users go through slices very quickly, as new anchor points are likely to generate in every slice due to change of object's size and location. As a result, blinking effect may produce. To reduce this effect, anchor points should not be changed as long as possible. However, this may cause

non-salient anchor points for objects. The system remembers the anchor points of the previous slice. After computing new anchor points for current slice, it compares them with previous positions. If positions are not changes for a certain thresh-hold value, previous positions are used. Label positions are unlikely to change much for unchanged anchor points. As a result, labels do not jump much (Fig. 5).

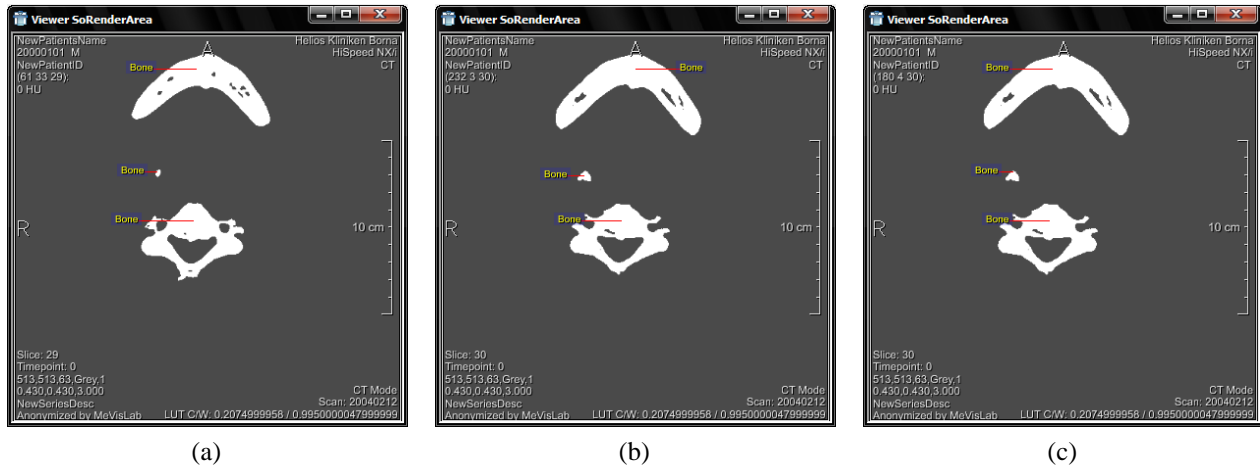


Figure 5: With no slice coherency, slice 29 (a) and slice 30 (b) have different label positions, while, with anchor point stabilization approach, slice 29 (a) and slice 30 (c) have almost similar label positions thus minimizes blinking effects.

5 Results and Discussion

The system is developed using MeVisLab, a medical data visualization tool based on QT framework and Open Inventor toolkits. The primary goal of the system is to generate external labels for CT slices which would help doctors and medical students to recognize different objects within the slices easily. So, for such system, perfect evolution should be empirical, i.e. users' feedback. Unfortunately, as the system is still in developing phase, no real-world user feedback is available. From the numerical point of view, four segmented CT images were used to generate labels with total 154 slices (Table 1). Among 1074 objects, all were labeled successfully. Because of attractive forces among objects and anchor points, it is seen that labels overlapped with objects (2.14%) are slightly more than while no force-directed method is used (1.49%). Though, both figures are very low, if compare to a number of total objects. There is only 0.1% line intersection which is a great result for readability and clarity. As there are usually less than 30 objects per slice, current standard computers take less than 2 seconds to generate labels for a slice. Even force-directed method takes insignificant time. So, the system is very suitable for real-time application.

Table 1: Summary of experimental results

No. of CT images = 4 Total slices =154 Total objects =1074 Failure to label = 0
With Non-grouping labeling No. of label overlap (no force)=12 No. of line Intersect (no force)=02 No. of label overlap (with force)=16 No. of line Intersect (with force)=03
With grouping labeling No. of line intersect=02 No. of label overlap each other=0 No. of label overlap with objects (no force) = 16 (1.49%) No. of label overlap with objects (with force) = 23 (2.14%)

6 Future Work and Conclusion

Generating textual labels dynamically for CT slices are very helpful for both doctors and medical students. As usual, there are always some scopes for future extensions of the work. The system currently only uses left-right flash layout. It can be extended for other labeling layouts like top-bottom, ring, radial etc. The system uses 2D texts for labeling. Using 3D texts in future more features like text zooming, rotating etc. can be added. Another good extension would be contextual grouping where objects with similar functionalities can be labeled together. Interactivity can be added so that users can choose which functional objects will be labeled.

ACKNOWLEDGMENT

The author thanks Prof. Bernhard Preim, Faculty of Informatics, OvG University of Magdeburg, Germany for lab facilities and input source images.

REFERENCES

- [1] K. Ali, K. Hartmann, & T. Strothotte, "Label layout for interactive 3D illustrations" in Journal of the WSCG, 13:1–8, 2005.
- [2] Carlo Arcelli and Gabriella Sanniti di Baja, "Finding local maxima in a pseudo-euclidean distance transform" in Computer Vision, Graphics and Image Processing, 43(3):361–367, 1988.
- [3] B. Bell and S. Feiner, "Dynamic space management for user interfaces" in Proceedings of Symposium on User Interface Software and Technology, p 238–248, 2000.
- [4] W. Chigona, H. Sonnet, F. Ritter, and T. Strothotte, "Shadows with a message" in Smart Graphics: Third International Symposium on Smart Graphics 2003, pp. 91–101. Springer Verlag, Berlin, 2003.

- [5] M. B. Dillencourt, H. Samet, and M. Tamminen, "A general approach to connected-component labeling for arbitrary image representations" in J. ACM 39(2), pp. 253–280, 1992.
- [6] M. Formann and F. Wagner. "A packing problem with applications to lettering of maps" in ACM Symp. on Comp. Geometry, volume 7, pages 281–288, 1991.
- [7] T.M.J. Fruchterman and E.M. Reingold, "Graph drawing by force-directed placement" in Software-Practice and Experience, 21(11):1129– 1164, 1991.
- [8] Furnas, G.W. "Generalized fisheye views", Proc. ACM SIGCHI'86 Conference on Human Factors in Computing Systems, Boston, April, pp. 16-23, 1986
- [9] T. Götzelmann, K. Hartmann, and T. Strothotte "Annotation of animated 3D objects" in Online Proc. 18th Simulation and Visualization Conference, Magdeburg, Germany, March 2007
- [10] K. Hartmann, K. Ali, and T. Strothotte, "Floating Labels: applying dynamic potential fields for label layout" in Smart Graphics: 4th International Symposium (SG 2004), pp. 101–113, 2004.
- [11] Ramesh Jain, Rangachar Kasturi, and Brian G. Schunck in Machine Vision, McGraw-Hill, Inc., 1995.
- [12] S. Loncaric and D. Kovacevic, "A method for segmentation of CT head images" in Proceedings of the 9th International Conference on Image Analysis and Processing, pp.388-395, FI., Italy, 1997
- [13] Z. Majcencic and S. Loncaric, "CT image labeling using simulated annealing algorithm" in Proceedings of the IX European Signal Processing Conference, Vol. 4, pp. 2513-2516, Island of Rhodes, Greece, 1998.
- [14] Thomas Porter and Tom Duff, "Compositing digital images" in Computer Graphics, 18(3), July 1984, 253-259
- [15] B. Preim, A. Raab, and Thomas Strothotte, "Coherent zooming of illustrations with 3D-graphics and text" in Proceedings of Graphics Interface, pages 105–113, 1997.
- [16] F. Ritter, H. Sonnet, K. Hartmann, and Th. Strothotte, "Illustrative Shadows: integrating 3D and 2D information displays" in International Conference on Intelligent User Interfaces, pages 166–173, 2003.
- [17] W. Rogers, Textbook of Anatomy, Churchill Livingstone, Edinburgh, 1992.
- [18] Rosenfeld and J. Pfaltz, "Distance functions in digital pictures" in Pattern Recognition, vol 1, p33–61,1968.
- [19] J. Sobotta, R. Putz, and R. Pabst, editors. *Sobotta: Atlas of Human Anatomy*. Volume 2: Thorax, Abdomen, Pelvis, Lower Limb. Williams & Wilkins, Baltimore, 12. English edition, 1997.
- [20] S. Oeltze-Jafra and B. Preim. (2014). *Survey of labeling techniques in medical visualizations*. In Proceedings of the 4th Eurographics Workshop on Visual Computing for Biology and Medicine (VCBM '14). Eurographics Association, Aire-la-Ville, Switzerland, Switzerland, 199-208. DOI=<http://dx.doi.org/10.2312/vcbm.20141192>.
- [21] Kang, Y.S., Park, S.H. & Joo, Y.J. Spat. Inf. Res. (2016) 24: 3. <https://doi.org/10.1007/s41324-016-0003-4>.